

Burial and exhumation cycles tracked by  $^{40}\text{Ar}/^{39}\text{Ar}$  and apatite (U-Th)/He  
thermochronology in a strike-slip fault zone, central Turkey

A Thesis

SUBMITTED TO THE FACULTY OF  
UNIVERSITY OF MINNESOTA  
BY

Lauren Idleman

IN PARTIAL FULFILLMENT OF THE REQUIREMENTS  
FOR THE DEGREE OF  
MASTER OF SCIENCE

Donna Whitney, Christian Teyssier

June 2013

© Lauren Idleman 2013

## **Acknowledgements**

Thanks to Donna Whitney, Christian Teyssier, Josh Feinberg, Annia Fayon, Michael Cosca (United States Geological Survey), Stuart Thomson (University of Arizona), Matthew Heizler (New Mexico Tech), and the members of the Structure, Tectonics, and Metamorphic Petrology research group

## Abstract

Muscovite and K-feldspar  $^{40}\text{Ar}/^{39}\text{Ar}$  ages from the eastern margin of the Niğde massif in central Anatolia document the timing of initial exhumation, reburial, and final exhumation and cooling of metamorphic rocks affected by deformation in the Central Anatolian Fault Zone, a long-lived strike-slip fault zone. Although the ages of initial and final cooling were known from previous studies, our new results document the timing of an intermediate thermal perturbation. Four of eight muscovite  $^{40}\text{Ar}/^{39}\text{Ar}$  samples have Late Cretaceous ages that date the initial cooling of high-grade metamorphic rocks at  $\sim 75$  Ma. The remaining four muscovite samples have perturbed spectra that climb to Late Cretaceous ages with increasing extraction temperatures. These four samples are located beneath a faulted unconformity overlain by Paleogene sedimentary rocks that were derived in part from the metamorphic massif, then buried and metamorphosed under greenschist facies conditions. Samples closer to the unconformity are more perturbed than structurally deeper samples. The age of the thermal perturbation is determined at 35-25 Ma using multi-diffusion domain modeling of  $^{40}\text{Ar}/^{39}\text{Ar}$  data from two K-feldspar-bearing gneiss samples, one located close to the unconformity, and one at a structurally deeper level. Muscovite  $^{40}\text{Ar}/^{39}\text{Ar}$  results and modeled K-feldspar temperature-time histories show that the eastern margin of the massif experienced a thermal pulse that peaked between 35-25 Ma after an initial cooling in the Late Cretaceous. Apatite (U-Th)/He (AHe) results track cooling from this perturbation, and indicate that the eastern margin of the massif had cooled to  $\sim 65^\circ\text{C}$  by  $\sim 19$  Ma. The thermal pulse has been attributed to the re-burial and heating of the eastern portion of the massif due to a period

of transpression across the Central Anatolian Fault Zone, which runs along the massif's eastern margin. Slip on the Central Anatolian Fault Zone at this time may be related to major tectonic events that were taking place in Central Anatolia, particularly the collision of Arabia with the Anatolian microplate.

## Table of Contents

List of figures .....	vii
<b>1. Introduction</b> .....	<b>1</b>
<b>2. Geologic Setting</b> .....	<b>3</b>
<b>3. The Niğde Massif</b> .....	<b>4</b>
<b>4. <math>^{40}\text{Ar}/^{39}\text{Ar}</math> Thermochronology</b> .....	<b>7</b>
4.1 Muscovite $^{40}\text{Ar}/^{39}\text{Ar}$ Methods .....	7
4.2 Muscovite $^{40}\text{Ar}/^{39}\text{Ar}$ Results .....	10
4.3 K-feldspar $^{40}\text{Ar}/^{39}\text{Ar}$ Methods .....	12
4.4 K-feldspar $^{40}\text{Ar}/^{39}\text{Ar}$ Results and Modeling .....	13
<b>5. Apatite (U-Th)/He Thermochronology</b> .....	<b>17</b>
5.1 Apatite (U-Th)/He Methods .....	17
5.2 Apatite (U-Th)/He Results .....	18
<b>6. Thermochronology Discussion</b> .....	<b>19</b>
<b>7. Burial and Exhumation History of the Niğde Massif</b> .....	<b>28</b>
<b>8. Conclusions</b> .....	<b>30</b>
<b>References</b> .....	<b>32</b>
<b>Appendices</b> .....	<b>37</b>
Appendix 1: Sample information .....	37
Appendix 2. Electron microprobe analyses of muscovite $^{40}\text{Ar}/^{39}\text{Ar}$ samples .....	38
Appendix 3. Muscovite $^{40}\text{Ar}/^{39}\text{Ar}$ results .....	39
Appendix 4. K-feldspar $^{40}\text{Ar}/^{39}\text{Ar}$ results .....	44
Appendix 5. Representative multi-diffusion domain model results for K-feldspar sample 11-TR-14 .....	47
Appendix 6. Representative multi-diffusion domain model results for K-feldspar sample 11-TR-18 .....	51
Appendix 7. Apatite (U-Th)/He results .....	55
Appendix 8. Plots of AHe age data .....	57

## List of Figures

<b>Figure 1</b> .....	2
<b>Figure 2</b> .....	6
<b>Figure 3</b> .....	8
<b>Figure 4</b> .....	9
<b>Figure 5</b> .....	17
<b>Figure 6</b> .....	19
<b>Figure 7</b> .....	14
<b>Figure 8</b> .....	15
<b>Figure 9</b> .....	20
<b>Figure 10</b> .....	28

## 1. Introduction

Although large lateral displacements may occur along strike-slip fault zones, localized or distributed transpression and transtension can also trigger significant vertical motion (Molnar, 1992; Teyssier et al., 1995; Okay et al., 2004; Spotila et al., 2007), including multiple cycles of burial and exhumation (yo-yo tectonics) (Umhoefer et al., 2007). However, identifying multiple burial and exhumation cycles in the geologic record can be challenging. Where possible, paired basin-basement studies are useful because basin deposits may record burial/heating events that post-date initial cooling and exhumation of basement rocks. Determining the timing of vertical motions (burial and exhumation) of rocks in a strike-slip fault zone provides temporal information (such as age, duration, and rates) about transpression and transtension episodes.

Although few good examples of yo-yo tectonics have been described, one locality where multiple cycles of burial and exhumation have been identified is the Niğde massif in central Turkey (Umhoefer et al., 2007; Whitney et al., 2007; 2008) (Fig. 1). The Niğde massif's two cycles of burial and exhumation may be related in part to interactions with the Ecemiş Fault, the southern segment of the Central Anatolian Fault Zone (CAFZ) that is adjacent to the massif's eastern margin at current levels of exposure (Fig.1). In the middle-late Pliocene, motion along the Ecemiş Fault was strike-slip, but it evolved to be more extensional/transtensional by the Pliocene-Quaternary (Jaffey and Robertson, 2001). The early history of the Ecemiş Fault, however, is not well known, although there is evidence in high-grade structural features in the Niğde massif (e.g., mineral lineation



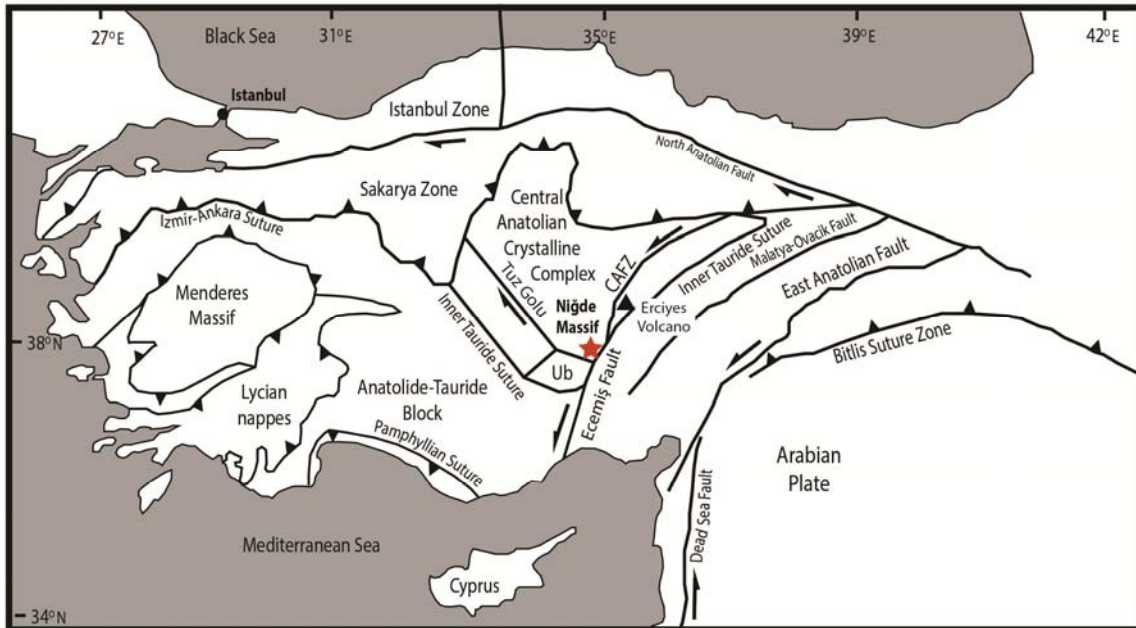


**Figure 1.** Simplified tectonic map of Turkey (after Umhoefer et al., 2007). The Niğde massif is located at the southern apex of the Central Anatolian Crystalline Complex (CACC) and is shown by a red star. The CACC is bounded by fault zones and sedimentary basins, including the Central Anatolian Fault Zone (CAFZ) along its eastern margin and the Ulukışla basin (Ub) to its south.

defined by sillimanite and biotite) for transpressional deformation in the orogenic middle crust (Whitney et al., 2001; 2007).

Previous workers have suggested that two episodes of transpression and transtension occurred along the Ecemiş Fault, resulting in cycles of burial and exhumation of the Niğde massif (Umhoefer et al., 2007; Whitney et al., 2007; 2008). Although the timing of initial and final cooling is documented by published  $^{40}\text{Ar}/^{39}\text{Ar}$  thermochronology data (Gautier et al., 2002; Whitney et al., 2003), the timing, magnitude and rate of the second cycle of burial and exhumation are only approximately known. New muscovite  $^{40}\text{Ar}/^{39}\text{Ar}$  and apatite (U-Th)/He ages from the eastern margin of the Niğde massif and modeling of new K-feldspar  $^{40}\text{Ar}/^{39}\text{Ar}$  data track the timing of thermal

and tectonic events associated with the reburial and final cooling and exhumation of the massif.

## **2. Geologic Setting**

Central Turkey is comprised of a composite metamorphic and plutonic massif known as the Central Anatolian Crystalline Complex (CACC) (Akıman et al, 1993) (Fig.1). The CACC is surrounded by suture zones formed from the subduction of strands of Neotethys during the Late Cretaceous (northern strand) to Eocene (southern strand) (Şengör and Yılmaz, 1981; Robertson and Dixon, 1984; Okay and Tüüzüs, 1999). Metamorphism and magmatism in the CACC occurred at 91-78 Ma (Kadioğlu et al., 2003; Whitney et al., 2003; Whitney and Hamilton, 2004; Boztuğ et al., 2008). In the late Oligocene to early Miocene, Arabia began to collide with Eurasia (Hempton, 1987; Beydoun et al., 1992; McQuarrie et al., 2003; McQuarrie and van Hinsbergen, 2013). The continued northward motion of the Arabian plate relative to Anatolia drives collision in eastern Anatolia, and is likely related to the formation of tectonic escape structures such as the North and East Anatolian strike-slip fault zones, which currently accommodate the bulk of western motion of the Anatolian plate (McKenzie, 1976; Le Pichon et al., 1995; Cianetti et al., 1997; Lundgren et al., 1998).

The modern CACC is comprised of the Kırşehir, Akdağ, and Niğde metamorphic massifs and is bounded on its western and eastern sides by strike-slip faults located in or near Neotethyan suture zones (Fig. 1). The sinistral Central Anatolian Fault Zone (CAFZ) and the dextral Tuz Gölü Fault define its eastern and western boundaries, respectively

(Fig. 1). The modern trace of the CAFZ strikes approximately N-S in the south (Ecemiş Fault), and then bends to a more NE-SW trend north of the Erciyes stratovolcano (Fig. 1). The Ecemiş Fault, the southern portion of the CAFZ, may have formed due to the oblique collision of the Tauride and Anatolide blocks during Anatolian assembly (Koçyiğit and Beyhan, 1998; Clark and Robertson, 2005). Estimates of Cenozoic offset along the CAFZ range from 60 km (Jaffey and Robertson, 2001) to 80 km (Koçyiğit and Beyhan, 1998). The CAFZ is seismically active today, particularly along its northern segment (Koçyiğit and Beyhan, 1998).

### **3. The Niğde Massif**

The Niğde metamorphic massif, located at the southern tip of the CACC, is a structural dome comprised of a high-grade core containing migmatitic metasedimentary rocks overlain by a carapace of marble, amphibolite, calc-silicate, quartzite and orthogneiss. All of these metamorphic units are intruded by the Üçkapılı granite (zircon U-Pb age = 92-85 Ma; Whitney et al., 2003). Metamorphic mineral lineation patterns in most of the massif, including the migmatitic core, are highly organized, NNE-trending and shallowly dipping. However, mineral lineation patterns in the eastern portion of the massif are highly disorganized, possibly due to block rotation (Whitney et al., 2007).

Along the eastern and southern margin of the Niğde massif, Cenozoic sedimentary deposits overlie the high-grade metamorphic rocks (Fig. 2). The contact between the sedimentary rocks and the massif has been described by some authors as a nonconformity (Gautier et al., 2002; 2008) and by others as a low-angle normal fault

(Whitney and Dilek, 1997; Fayon et al., 2001) or faulted unconformity (Umhoefer et al., 2007).

The Niğde massif was metamorphosed to upper amphibolite facies (Whitney and Dilek, 1998; Whitney et al., 2001), intruded by granite, and cooled rapidly to  $\leq 350^{\circ}\text{C}$  during the Late Cretaceous (Whitney et al., 2003; Umhoefer et al., 2007; Gautier et al., 2008). Previously published  $^{40}\text{Ar}/^{39}\text{Ar}$  hornblende, white mica, and biotite data from the core of the massif are similar in age and have clearly-defined plateaus (Whitney et al., 2003; 2007; Umhoefer et al., 2007; Gautier et al., 2008).  $^{40}\text{Ar}/^{39}\text{Ar}$  ages for mica from the eastern margin of the massif, however, lack clearly defined plateaus and show a marked disturbance of their  $^{40}\text{Ar}/^{39}\text{Ar}$  systematics. There is a clear spatial correlation between the perturbed  $^{40}\text{Ar}/^{39}\text{Ar}$  and disorganized mineral lineations (Whitney et al., 2007). Owing to this association, Umhoefer et al. (2007) proposed that the massif be divided into an eastern belt (disorganized mineral lineation patterns; perturbed  $^{40}\text{Ar}/^{39}\text{Ar}$  spectra) and western belt (organized mineral lineation patterns; concordant  $^{40}\text{Ar}/^{39}\text{Ar}$  spectra) (Fig. 3).

The perturbation of the  $^{40}\text{Ar}/^{39}\text{Ar}$  spectra may be related to the tectonic/thermal events that metamorphosed the sedimentary deposits overlying the Niğde massif. These events have been linked to burial and exhumation cycles (yo-yo tectonics) associated with motion on the Ecemiş Fault (Umhoefer et al., 2007). According to this model, an initial cycle of burial and exhumation occurred in the Late Cretaceous, when supracrustal rocks were buried and metamorphosed to upper amphibolite facies conditions to form the high-grade core of the massif. These rocks were exhumed to the surface by the Paleogene, as indicated by the presence of Paleocene-Eocene sedimentary units that were

unconformably deposited onto the metamorphic rocks (Yetiş et al., 1995; Gautier et al., 2002). Field and petrologic evidence shows that these sedimentary deposits were deformed and metamorphosed under greenschist facies conditions (Umhoefer et al., 2007).

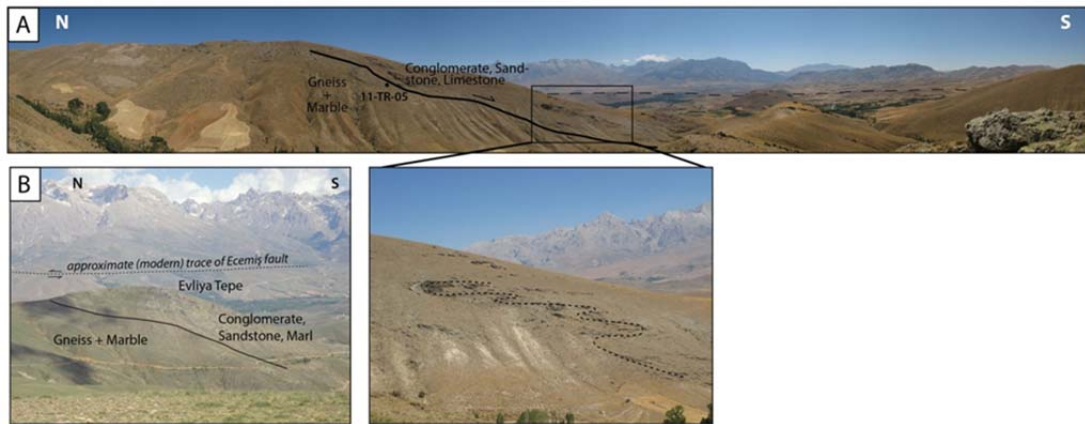


**Figure 2.** **A)** Field photo of Ortatepe Ridge. The contact between metamorphic basement rocks of the Niğde massif and overlying basin rocks is a faulted unconformity with normal sense displacement. The sedimentary rocks above the contact are strongly deformed and asymmetrically folded in this area (see inset for detail). **B)** Evliya Tepe section, where samples 11-CAT-06 and 11-CAT-07 were collected. Metasedimentary rocks above the contact are deformed but not strongly folded in this region.

Apatite fission track ages show that final cooling of Niğde metamorphic rocks and metamorphosed sedimentary basin deposits to 120-60°C occurred by ~19-9 Ma (Fayon et al., 2001; Umhoefer et al., 2007); most ages from the structurally deepest part of the massif are 11-12 Ma. Thermal modeling of apatite fission track age and track length data demonstrated that these ages likely record exhumation-related cooling in the Miocene and have not been significantly affected by thermal effects from volcanic deposits or other magmatic activity (Fayon and Whitney, 2007).

#### 4. $^{40}\text{Ar}/^{39}\text{Ar}$ Thermochronology

In this study,  $^{40}\text{Ar}/^{39}\text{Ar}$  dating of muscovite from the eastern belt of the Niğde massif was undertaken in order to determine the magnitude and timing of a Cenozoic thermal event.  $^{40}\text{Ar}/^{39}\text{Ar}$  dating of K-feldspar was also utilized. Multi-diffusion domain modeling of  $^{40}\text{Ar}/^{39}\text{Ar}$  results from two K-feldspar samples from the eastern belt yielded temperature-time histories that span a temperature range from  $\sim 150\text{-}300\text{ }^{\circ}\text{C}$ . This temperature range captures a detailed history of the thermal pulse that only partially perturbed the  $^{40}\text{Ar}/^{39}\text{Ar}$  system in muscovite ( $T_c = \sim 400\text{-}425\text{ }^{\circ}\text{C}$ ; Hames and Bowring, 1994; Kirschner et al., 1996, Harrison et al., 2009).

##### 4.1 *Muscovite $^{40}\text{Ar}/^{39}\text{Ar}$ Methods*

Eight muscovite-bearing gneiss samples were collected from metamorphic rocks in the eastern belt of the Niğde massif along a transect from the faulted unconformity to structurally deeper levels at the boundary between the eastern and western belts (Fig. 3; see appendix 1 for sample information). These rocks have muscovite grain sizes of  $\sim 0.5\text{-}1.5\text{ mm}$ , although one sample, 11-TR-03, had larger ( $\sim 2\text{-}3\text{ mm}$ ) muscovite grains (Fig. 4a). Muscovite crystals in these rocks commonly display ragged edges and some are intergrown with biotite. In samples collected near the faulted unconformity, muscovite grains are locally crosscut by pervasive, thin-section scale fractures (Fig. 4b) and commonly show undulose extinction, but do not exhibit other symptoms of deformation. Electron microprobe analyses of white micas in these rocks reveal little variation in muscovite compositions and a lack of compositional zoning (appendix 2).

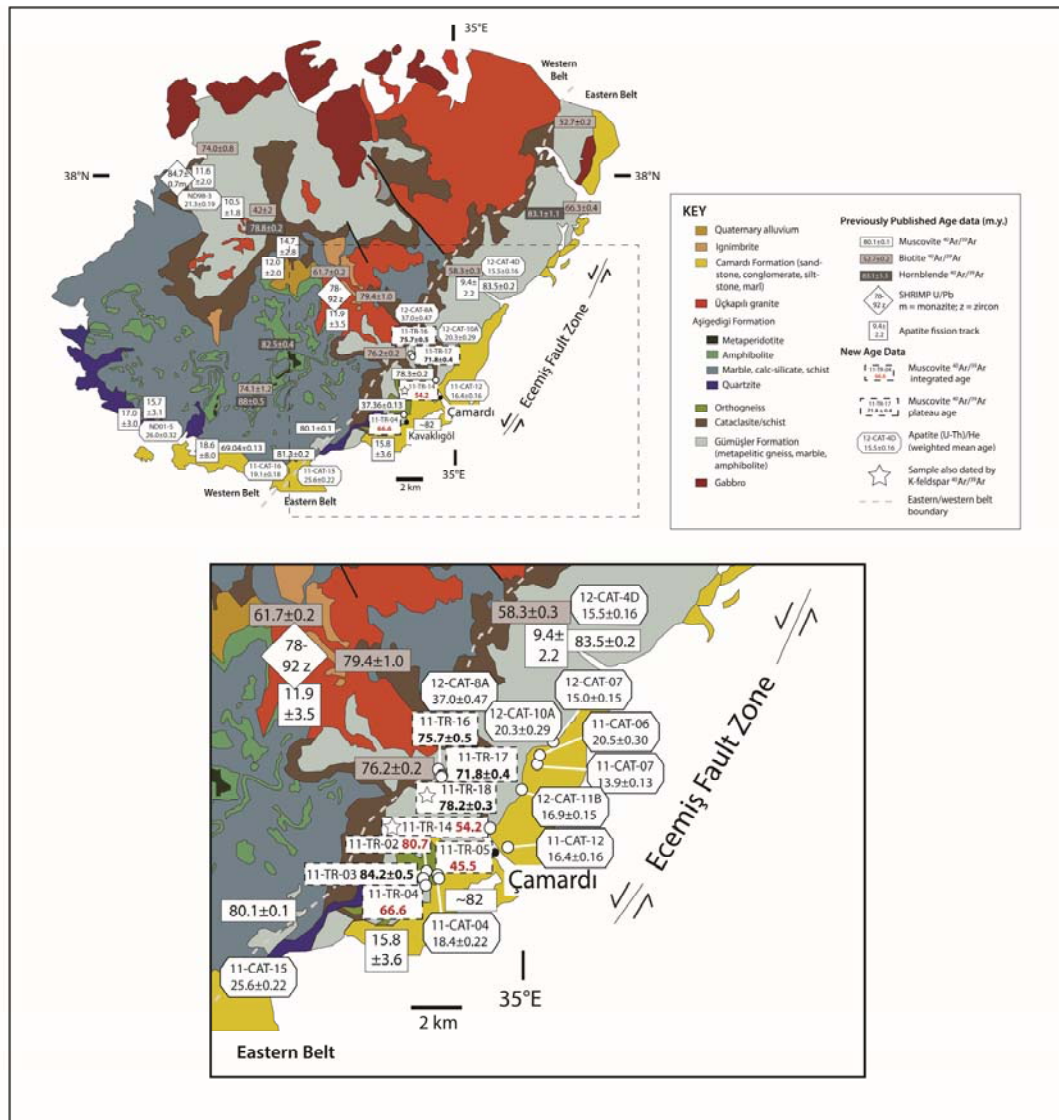


**Figure 3.** Geologic map of the Niğde Massif with representative previously published thermochronology data (Fayon et al., 2001; Whitney et al., 2003; Umhoefer et al., 2007) and new age data from this study. Inset shows detail of the SE region of the massif, including new white mica  $^{40}\text{Ar}/^{39}\text{Ar}$  and apatite (U-Th)/He ages.

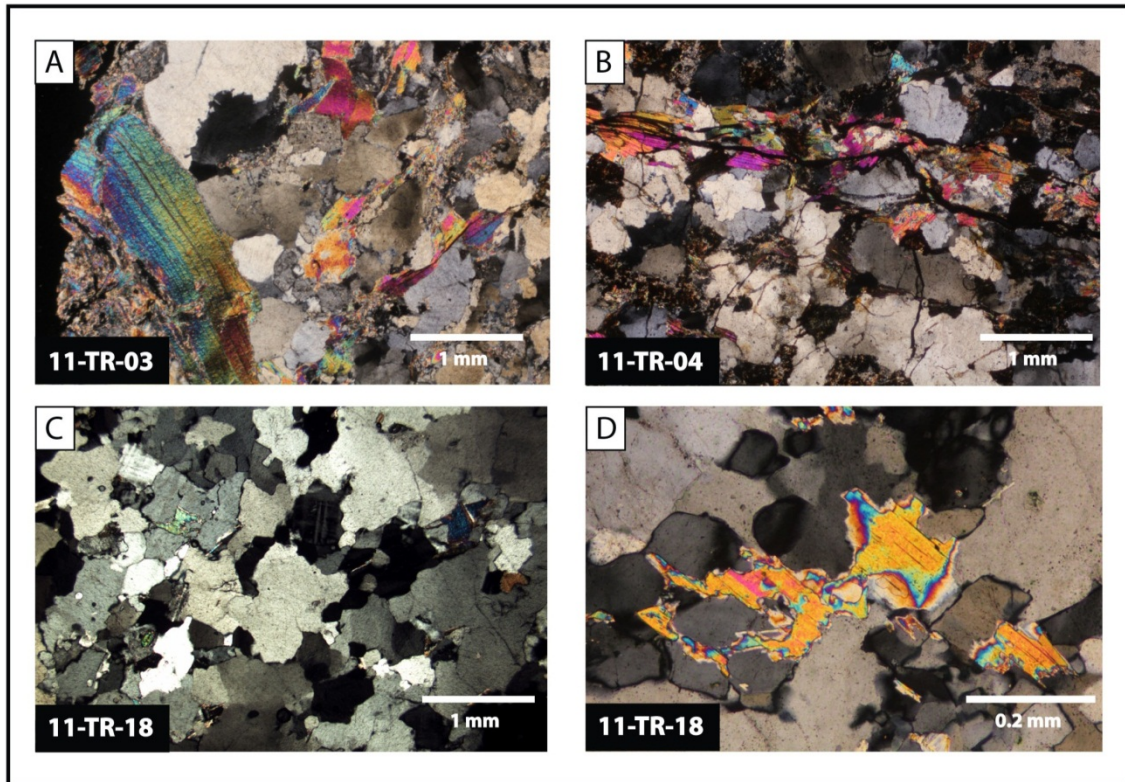


**Figure 4.** Photomicrographs of white mica and K-feldspar  $^{40}\text{Ar}/^{39}\text{Ar}$  samples. **A)** Sample 11-TR-03 (gneiss). A single large muscovite grain from this sample was dated by  $^{40}\text{Ar}/^{39}\text{Ar}$ . The large muscovite grain pictured here showed weak undulatory extinction, and showed several fractures. The fractures in this sample occurred near grain boundaries, and therefore did not significantly reduce the diffusion length scale for  $^{40}\text{Ar}$  in this sample (see text for discussion of deformation-enhanced  $^{40}\text{Ar}$  loss in muscovite) **B)** Sample 11-TR-04 (cataclasite /gneiss); dated by white mica  $^{40}\text{Ar}/^{39}\text{Ar}$ . This sample contained pervasive thin section scale fractures that occasionally cross-cut muscovite grains, shown here. **C)** and **D)** Sample 11-TR-18 (leucogneiss); dated by white mica and K-feldspar  $^{40}\text{Ar}/^{39}\text{Ar}$ . This sample contained few (~3-5) muscovite grains and had little fracturing compared to samples located close to the unconformity between metamorphic rocks and Camardi sedimentary rocks.

Muscovite mineral separates were prepared using standard mineral separation techniques at the University of Minnesota. Visibly altered grains were removed during hand picking to ensure clean mineral separates. Aliquots of 1-3 grains were packaged and irradiated at the USGS TRIGA reactor using the Fish Canyon Tuff sanidine (28.201 Ma; Kuiper et al., 2008) as a neutron flux monitor. The muscovite samples were analyzed at



the USGS  $^{40}\text{Ar}/^{39}\text{Ar}$  Geochronology Laboratory in Denver, CO on a Mass Analyzer Products 215-50 mass spectrometer using an infrared ( $\text{CO}_2$ ) laser as the heating source.

#### 4.2 Muscovite $^{40}\text{Ar}/^{39}\text{Ar}$ Results

Eight muscovite  $^{40}\text{Ar}/^{39}\text{Ar}$  ages from the eastern belt of the Niğde massif are presented here (Figs. 3, 5; appendix 3). Plateau ages were determined for samples 11-TR-03, 11-TR-16, 11-TR-17, and 11-TR-18. Plateaus were defined when the ages of successive thermal extraction steps comprising 50% of the total  $^{39}\text{Ar}$  released overlapped at  $2\sigma$  error. Four of the eight reported ages (for samples 11-TR-02, 11-TR-04, 11-TR-05, and 11-TR-14) show a marked disturbance in their  $^{40}\text{Ar}/^{39}\text{Ar}$  systematics, and a total gas age is reported for these samples. Of these samples, three display a “staircase pattern,” with ages that increase systematically with increasing laser power. The lower laser power steps for these samples yield ages ranging from ~25 to 35 Ma, and successive steps climb to ages of ~65 to 85 Ma. The remaining four samples display a series of successive steps that yield similar ages, although several of these samples also display younger ages at lower laser power steps. While these samples do not display statistically rigorous plateau, a weighted mean age for successive steps of similar age is reported.

The samples that show the most marked disturbance in the  $^{40}\text{Ar}/^{39}\text{Ar}$  system tend to be those located closest to the eastern margin of the Niğde massif, adjacent to the faulted unconformity between the basement rocks and metasediments of the Çamardı formation (11-TR-04 and 11-TR-14) (Figs. 5, 6). Samples collected from structurally

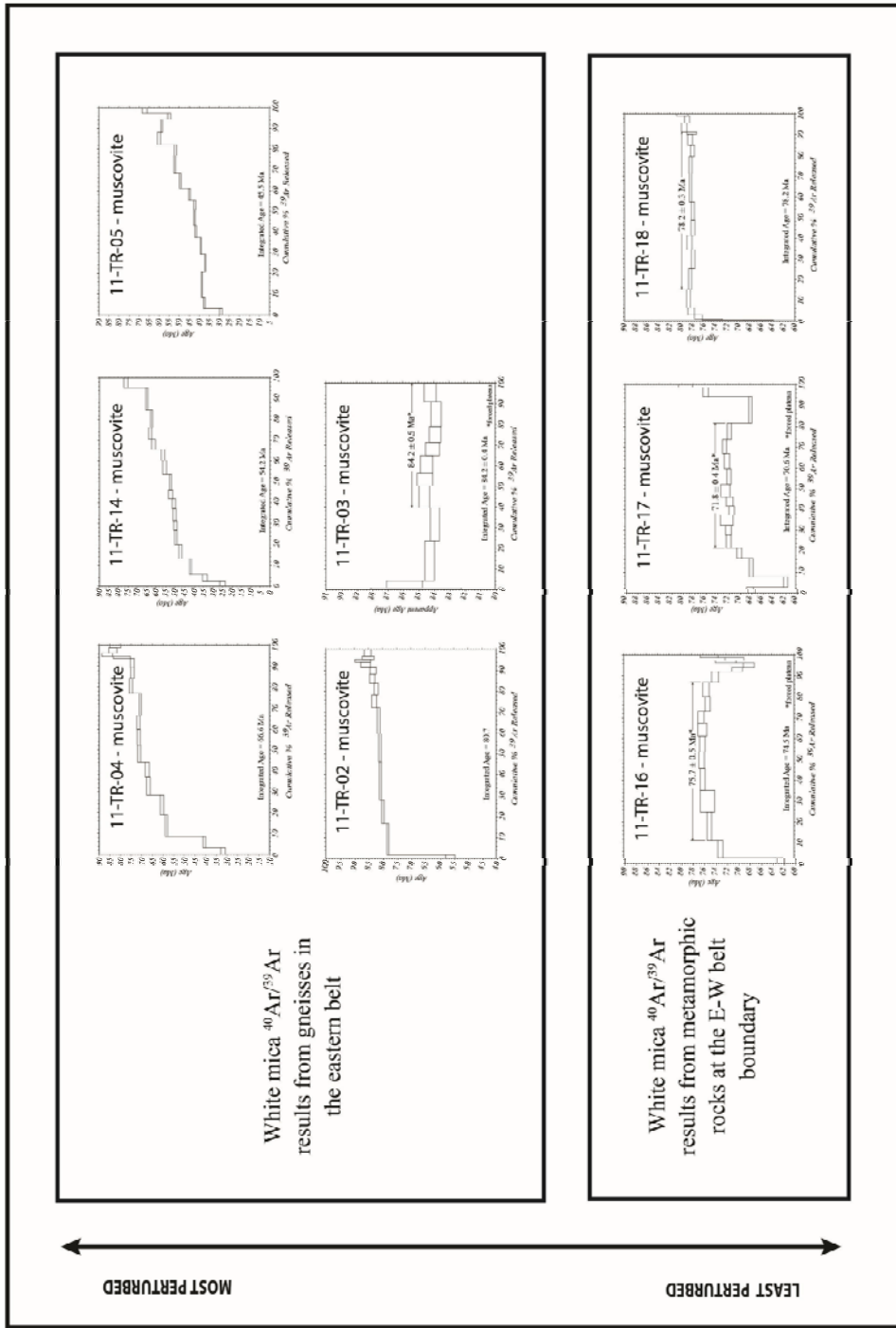


**Figure 5.** Muscovite  $^{40}\text{Ar}/^{39}\text{Ar}$  results for the eastern margin of the Niggde Massif, arranged in order of increasing structural depth. Samples that correspond to shallower structural depths have  $^{40}\text{Ar}/^{39}\text{Ar}$  spectra that are the most perturbed.

deeper levels (11-TR-02, 11-TR-03, and 11-TR-05) were also discordant, although less so than the easternmost samples (Figs. 5, 6). One exception to this trend is sample 11-TR-03, which yielded a broadly similar muscovite result with a plateau age of  $84.2 \pm 0.5$  Ma. The three structurally deepest samples, located near the proposed boundary between the eastern and western belts (11-TR-16, 11-TR-17, and 11-TR-18), all yielded reasonably similar results with plateau ages of  $75.7 \pm 0.5$  Ma,  $71.8 \pm 0.4$  Ma, and  $78.2 \pm 0.3$  Ma, respectively.

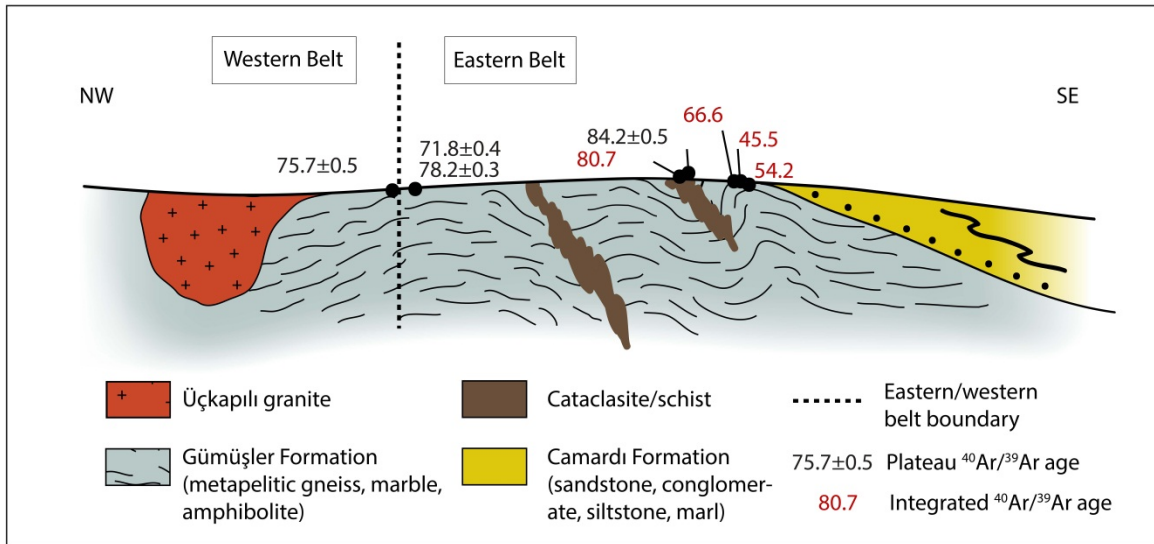


**Figure 6.** Conceptual cross-section of a portion of the Niğde Massif showing muscovite  $^{40}\text{Ar}/^{39}\text{Ar}$  ages from this study. Samples located adjacent to the E-W belt boundary tend to have similar Late Cretaceous ages, while those farther east are perturbed and commonly have younger ages.

#### 4.3 *K-feldspar* $^{40}\text{Ar}/^{39}\text{Ar}$ Methods

K-feldspar grains from two gneiss samples, 11-TR-14 and 11-TR-18, were dated by  $^{40}\text{Ar}/^{39}\text{Ar}$  (Fig. 3, appendix 4). These samples were chosen because of their strategic locations: 11-TR-14 is located adjacent to the unconformity between the metamorphic

core of the massif and the Çamardı formation, while 11-TR-18 is located further west, along the E-W belt boundary. K-feldspar in these samples have sutured grain boundaries and are ~0.5 mm in diameter (Fig. 4c). K-feldspar grains in these samples are readily identifiable by their tartan twinning.

K-feldspar mineral separates were irradiated for 20 hours at the UGGS TRIGA reactor in Denver, CO along with the standard Fish Canyon tuff sanidine (28.02 Ma; Renne et al., 1998) as a neutron flux monitor. The  $^{40}\text{Ar}/^{39}\text{Ar}$  analyses were undertaken at the New Mexico Geochronology Research Laboratory. The separates were heated within a double vacuum Nb resistance furnace and the evolved argon was analyzed using a fully-automated Mass Analyzer Products 215-50 mass spectrometer.

#### *4.4 K-feldspar $^{40}\text{Ar}/^{39}\text{Ar}$ Results and Modeling*

Age spectra for K-feldspar from gneiss samples 11-TR-14 and 11-TR-18 are characterized by large age gradients. The age spectra start at ~ 25 Ma, and climb monotonically to 70-75 Ma (Figs 7b, 8b). The first few percent of total gas release yields anomalously high ages that may be related to the release of excess  $^{40}\text{Ar}$  trapped in fluid inclusions (Harrison et al., 1993). The samples are highly radiogenic and typical of K-feldspar; however, the bulk sample is relatively low in total K (~4-8%; appendix 4), suggesting either contamination of the mineral separate by quartz or intermediate composition alkali feldspar. Petrographic observations show that feldspars in these samples are predominantly microcline and did not reveal the presence of albite exsolution (Fig. 4c). K/Ca values range between about 25 and 100.

Laboratory heating results from these two feldspar samples were modeled using the multi-diffusion domain (MDD) method (Lovera et al., 1989). A modified version of the routine AutoArr (programmed by Oscar Lovera, <<http://sims.ess.ucla.edu/argonlab/>>

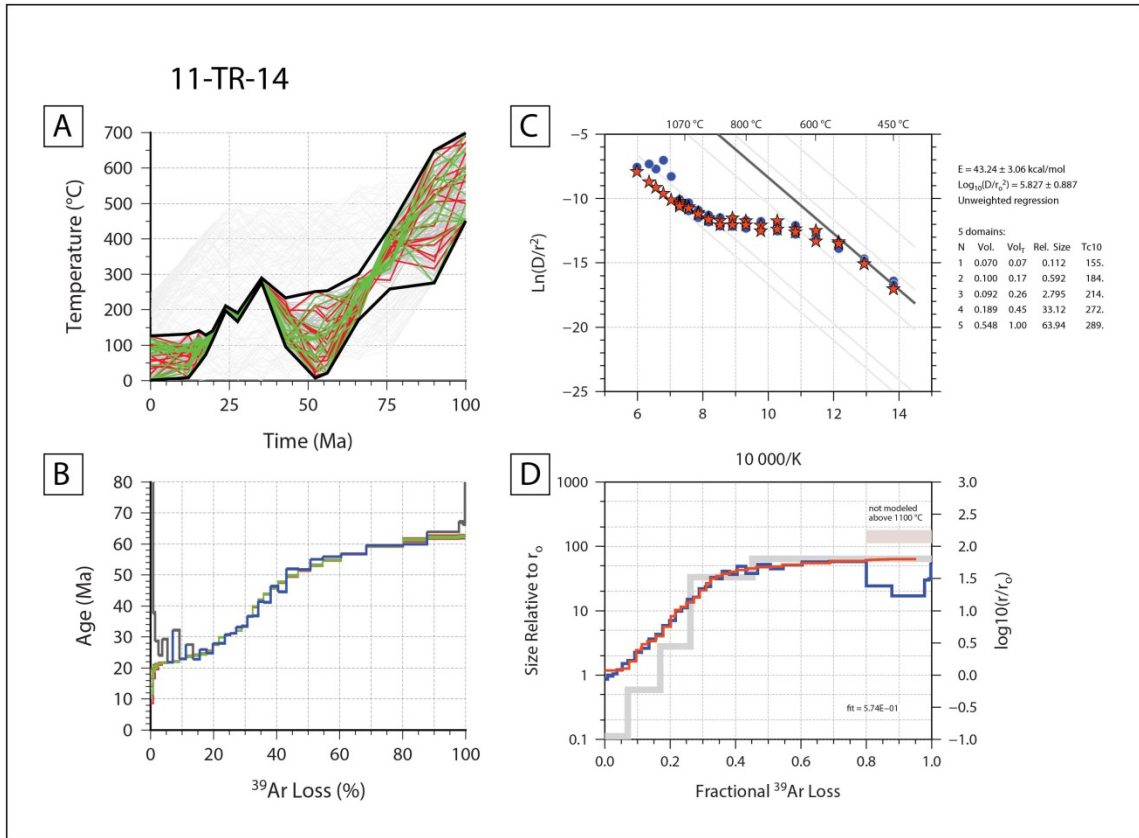


**Figure 7.** Kinetic data and preferred multi-diffusion domain ( MDD) model results for K-feldspar sample 11-TR-14. **A)** Temperature-time history generated by Arvert 4.1. Green lines represent the fifteen best-fitting thermal histories; red represent the fifteen worst-fitting thermal histories, and gray lines are all intermediate thermal histories in the final pool. Light gray lines outside the solution envelope represent thermal histories in the initial Monte Carlo pool. Re-heating was allowed during model runs. **B)** Comparison between measured age spectrum (blue) and model age spectrum generated from the best-fitting (green) and worst-fitting (red) thermal histories in (A). Gray portions of the blue age spectrum represent steps that are affected by excess argon and were not included in the model when generating temperature-time histories. **C)** Arrhenius plot for 11-TR-14 (blue) with MDD model (red stars) Activation energy determined from the slope of the lowest-temperature initial linear array (black). **D)** Measured  $r/r_0$  spectra for sample 11-TR-14 (blue) along with the modeled  $r/r_0$  spectra (red) and modeled domain sizes (gray). Domains were not modeled beyond the melting point of the sample (~1150°C).

programs/Readme-autoarr.html>) was used to determine the best-fit diffusion domain structure and diffusion parameters based on the  $^{39}\text{Ar}$  laboratory release data for the two K-feldspar samples from the Niğde massif. The domain structures and diffusion

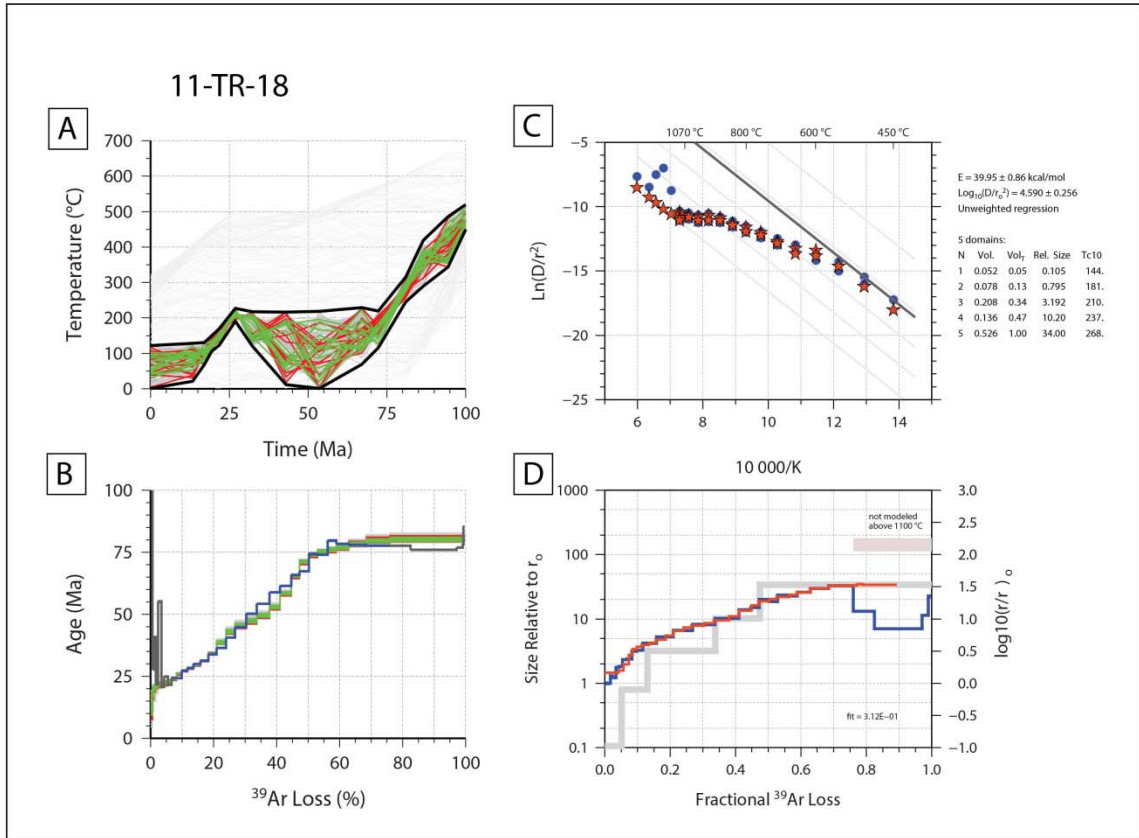


**Figure 8.** Kinetic data and preferred multi-diffusion domain (MDD) model results for K-feldspar sample 11-TR-18. **A)** Temperature-time history generated by Arvert 4.1. Green lines represent the fifteen best-fitting thermal histories; red represent the fifteen worst-fitting thermal histories, and gray lines are all intermediate thermal histories in the final pool. Light gray lines outside the solution envelope represent thermal histories in the initial Monte Carlo pool. Re-heating was allowed during model runs. **B)** Comparison between measured age spectrum (blue) and model age spectrum generated from the best-fitting (green) and worst-fitting (red) thermal histories in (A). Gray portions of the blue age spectrum represent steps that are affected by excess argon and were not included in the model when generating temperature-time histories. **C)** Arrhenius plot for 11-TR-14 (blue) with MDD model (red stars) Activation energy determined from the slope of the lowest-temperature initial linear array (black). **D)** Measured  $r/r_0$  spectra for sample 11-TR-14 (blue) along with the modeled  $r/r_0$  spectra (red) and modeled domain sizes (gray). Domains were not modeled beyond the melting point of the sample ( $\sim 1150^\circ\text{C}$ ).

coefficients were entered into Arvert 4.1 (Programmed by Peter Zeitler, <<http://www.ees.lehigh.edu/EESdocs/geochron/software.html>>), an inverse modeling program that generates a series of plausible thermal histories for each sample by attempting to fit modeled age spectra to the measured age spectra. The algorithm performs a constrained random search by minimizing the mismatch between the age spectra that result from modeled thermal histories and the experimentally determined age spectrum. With each iteration, poorly fitting age spectra are discarded and the remainder are inverted and re-investigated, eventually resulting in a collection of plausible thermal histories.

The initial pool of thermal histories (150 in these model runs) generated by Arvert 4.1 obeys a set of initial T-t and heating/cooling rate constraints set by the operator. The preferred thermal history for sample 11-TR-14 had T-t constraints of 450-700°C at 100 Ma, 100-600°C at 80 Ma, 0-500°C at 50 Ma, 0-500°C at 25 Ma, and 0-250°C at 0 Ma. The histories in the initial Monte Carlo pool were allowed to heat and cool at 15°C/m.y. and the final constrained random search (CRS) pool was allowed to heat and cool at 25°C/m.y. The preferred thermal history for sample 11-TR-18 was generated using the following T-t constraints: At 100 Ma, temperatures were restricted to 450-700°C; at 80 Ma, to 0-600°C; at 50 Ma, to 0-500°C; at 25 Ma, to 0-500°C; and at 0 Ma, to 0-250°C. The histories in the initial Monte Carlo pool were allowed to heat and cool at 5°C/m.y. and the final constrained random search (CRS) pool was allowed to heat and cool at 20°C/m.y. (see appendices 5 and 6 for a full description of model constraints used in the preferred T-t history and examples of other T-t histories generated for samples 11-TR-14 and 11-TR-18). In some instances, the model was run step-wise, allowing the

heating/cooling rate in subsequent Monte Carlo and CRS pools to increase gradually with each model iteration (see appendices 5 and 6 for results). The final thermal histories in the preferred T-t history for sample 11-TR-14 have < 2.71% mean error of fit to the age spectrum, and the final thermal histories for the preferred T-t history for 11-TR-18 have < 3.6% mean error of fit to the age spectrum.

The preferred MDD models of the  $^{40}\text{Ar}/^{39}\text{Ar}$  results from the two K-feldspar samples yield similarly-shaped T-t histories (Figs 7a, 8a). Both samples experienced cooling from high temperatures in the Late Cretaceous, followed by a period of quiescence before a re-heating event that peaked at 35-25 Ma. The samples cooled rapidly from this event, falling below the closure temperatures of their smallest domains (144 to 155°C) by 20-15 Ma (Figs 7a, 8a).

## **5. Apatite (U-Th)/He Thermochronology**

Apatite (U-Th)/He thermochronology (AHe) can record cooling through temperatures ~50-80°C (Farley, 2002). Because the K-feldspar T-t histories are insensitive to temperatures below ~150°C, the AHe results help define the final stages of the Niğde massif's cooling history.

### *5.1 Apatite (U-Th)/He Methods*

Apatite was separated from 13 rock samples using standard mineral separation techniques. Two of these samples are metamorphic rocks from the structurally deepest part of the Niğde massif (the migmatitic core of the proposed western belt), five from



metamorphic rocks in the eastern belt (likely structurally higher than the western belt), and six are from the Çamardı formation (metamorphosed basin deposits) (Fig. 3; appendix 7).

Individual apatite grains were prepared and analyzed at the University of Arizona Radiogenic Helium Dating Laboratory. Grains were examined optically and three grains with the fewest inclusions from each sample were selected for analysis. The dimensions of individual grains were measured using manually calibrated imaging software in order to apply  $\alpha$ -ejection corrections (following Hourigan et al., 2005). The grains were then packaged in 1-mm Nb foil envelopes and degassed by heating with a Nd-YAG laser. Concentration of  $^4\text{He}$  was determined by  $^3\text{He}$  isotope dilution and a quadrupole mass spectrometer. U, Th, and Sm concentrations were obtained by isotope dilution using an inductively coupled plasma mass spectrometer to calculate a raw age.

### *5.2 Apatite (U-Th)/He Results*

Apatite from the Çamardı formation yielded (U-Th)/He ages between ~26 and ~14 Ma (although five of six fell within ~20-14 Ma) (appendix 7). One sample collected at the E-W belt boundary (12-CAT-8A) has an anomalously old age of  $37.04 \pm 0.47$  Ma, possibly due to the presence of U-rich inclusions. This sample should have been re-set during the Oligocene re-heating event that was clearly recorded by a K-feldspar sample collected ~2.5 km to the south. There is no apparent systematic age/elevation or spatial age distribution in these samples (appendix 8).

Apatite He (AHe) results from many of the samples show a wide dispersion of ages between analyzed grains. There is no clear correlation between effective uranium content and grain age. Apatite grains from most samples tend to be small (short axis ~40-80  $\mu\text{m}$ ), have pitted surfaces and rounded shapes, and many lack euhedral terminations. In several cases, grain shards were the only inclusion-free material available and were utilized for dating despite their unfavorable morphology. The analysis of broken grains may be partially responsible for the age dispersion exhibited by some of these samples (Brown et al., 2011), along with other potential factors including U-Th rich inclusions not detected during grain picking, U-Th zoning, and enhanced He retention due to radiation damage (Fitzgerald et al., 2006). Owing to the limitations imposed by these samples, both individual grain ages and weighted mean ages for each sample are reported and the AHe data are treated in a general manner. Despite the issues with our apatite samples, the AHe ages from this study agree very well with apatite fission track ages from the Çamardı formation rocks that yielded ages of  $8.7 \pm 2.2$  Ma (Umhoefer et al., 2007).

## **6. Thermochronology Discussion**

The  $^{40}\text{Ar}/^{39}\text{Ar}$  results from four muscovite samples show evidence of partial resetting attributable to an Oligocene or younger thermal event. These samples have relatively young ages (25-35 Ma) at low-temperature laboratory outgassing steps that climb in staircase fashion to Late Cretaceous (70-85 Ma) ages with increasing laser power (Fig. 5). When all of the age spectra are plotted together, it is apparent that a thermal event that occurred no later than ~35-25 Ma affected these muscovite grains to varying degrees

(Fig. 9). The staircase pattern in  $^{40}\text{Ar}/^{39}\text{Ar}$  spectra from samples 11-TR-04, 11-TR-05, and 11-TR-14, and to a lesser extent, 11-TR-02, may have been caused by a number of factors. A simple diffusion gradient imposed on a single diffusion domain size (i.e., the entire mica grain) can produce staircase-shaped age spectra. Alternatively, deformation-enhanced  $^{40}\text{Ar}$  loss or mixing of a neoblastic mica population with an older, relic population can also cause this effect.

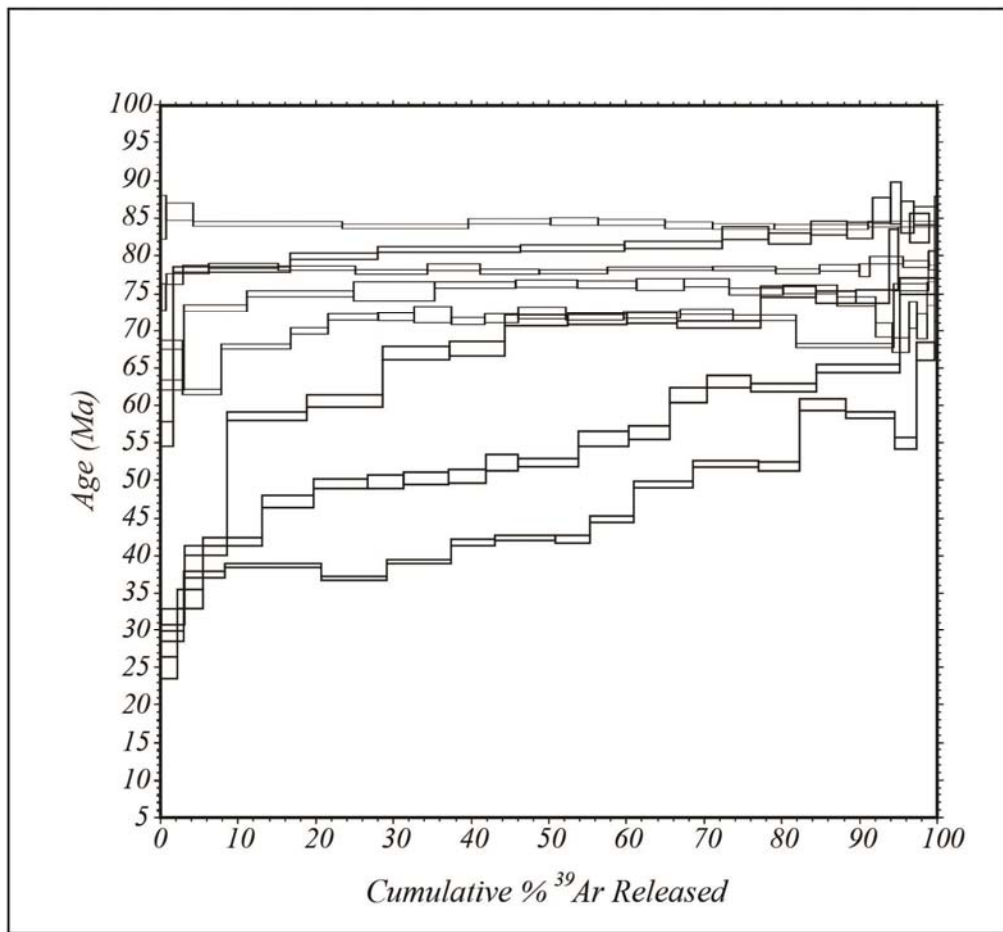


**Figure 9.** All muscovite  $^{40}\text{Ar}/^{39}\text{Ar}$  spectra on a single plot. Lower-temperature furnace steps from perturbed samples commonly show younger (25-35 Ma) ages that rise monotonically to Late Cretaceous (70-85 Ma) ages.

The cause of the staircase spectra in these samples has potentially important implications for determining the spatial extent of Oligocene heating. If the mica samples had the same Ar retentivity, then rocks located farther to the east must have experienced a deeper or more protracted reburial than their counterparts adjacent to the E-W belt boundary, which were at most minimally affected. Growth of neoblastic mica leading to staircase patterns in samples closest to the unconformity would also indicate a localized heating event. Alternatively, if intragrain deformation reduced the retentivity of some samples, then a regional heating event may have produced variable amounts of  $^{40}\text{Ar}$  loss in variably deformed samples despite uniform heating of all samples.

The muscovite samples located close to the faulted unconformity between the metamorphic rocks and the Çamardı basin metasedimentary rocks show the greatest degree of radiogenic  $^{40}\text{Ar}$  loss. Extensive thin-section scale fracturing and undulose extinction are observed in micas from samples near the unconformity. In some cases, the fractures locally cut through entire mica grains. Samples farther from the contact with the Çamardı basin metasedimentary rocks (those along the E-W belt boundary) have a lower mica content than those near the contact, but of those micas observed in thin section, the majority are undeformed and about one third show weak undulatory extinction as the only apparent deformational microstructure. Very few fractures are evident in these samples.

Deformation in muscovite has been shown to effectively shorten the length scale over which  $^{40}\text{Ar}$  diffuses, reducing the  $^{40}\text{Ar}$  retentivity of deformed muscovite grains and making them more susceptible to  $^{40}\text{Ar}$  loss during a reheating event (Kramar et al., 2001;

Cosca et al., 2011). However, the deformation documented in these studies is more intense (undulose extinction, extensive kinking, cracking, and the development of mica fish) than that observed in samples from the eastern margin of the Niğde massif (undulose extinction and occasional fracturing). It is unclear whether the relatively minor amount of deformation affecting these micas was sufficient to produce the degree of  $^{40}\text{Ar}$  loss experienced by samples closest to the unconformity. Furthermore, low sampling density and a lack of micas in samples from the E-W belt boundary makes it difficult to fully assess the spatial extent and intensity of muscovite deformation and conclusively correlate it with the  $^{40}\text{Ar}/^{39}\text{Ar}$  results.

It is also difficult to determine from the  $^{40}\text{Ar}/^{39}\text{Ar}$  results whether mixing of multiple mica populations has affected these samples, as the effects of multiple muscovite populations on  $^{40}\text{Ar}/^{39}\text{Ar}$  age spectra remain uncertain. Experimental mixing of two muscovite populations in various proportions has been found to yield reasonably flat age spectra that correspond to ages that fall between those of the two mixed populations (e.g., Kula et al., 2010), but can also produce staircase patterns (e.g. West and Lux, 1993). Although the  $^{40}\text{Ar}/^{39}\text{Ar}$  results don't rule out mica mixing, there is no compositional or petrographic evidence for multiple mica populations in these samples. A single, large (~2-3 mm) grain was analyzed from sample 11-TR-03, and the result definitively rules out mixing of multiple crystal populations for this sample. This sample, although close to the unconformity with the Çamardı Formation, yielded a flat plateau with a Late Cretaceous age ( $84.2 \pm 0.5$  Ma), despite petrographic evidence of undulose extinction in other large mica grains from this rock. In this instance, it is possible that

analyzed grain was undeformed, or that the amount of deformation was insufficient to cause significant  $^{40}\text{Ar}$  loss. The large mica grain size in this sample may make it particularly retentive of  $^{40}\text{Ar}$ , especially if the grain boundaries define a single diffusion domain.

Ultimately, it is not possible to definitively determine the cause of  $^{40}\text{Ar}$  loss observed in muscovite samples from the eastern margin of the Niğde massif given currently available information. Although the presence of multiple muscovite populations in these samples cannot be entirely ruled out, there is no compositional or petrographic evidence for it, making this scenario unlikely. Assuming that the mica grains in all of the analyzed samples represent single domains for  $^{40}\text{Ar}$  diffusion, a localized reheating event in the eastern portion of the massif could have produced significant diffusion gradients in micas from samples near the unconformity (and therefore closer to the CAFZ) that are reflected in their disturbed  $^{40}\text{Ar}/^{39}\text{Ar}$  age spectra. The anomalous, relatively undisturbed age spectrum obtained from nearby sample 11-TR-03 would then be attributed to its large grain size relative to the other samples. Alternatively, samples collected near the unconformity may have experienced enhanced  $^{40}\text{Ar}$  loss due to the development of deformational microstructures evident in thin section, although it is unclear whether the deformation is extensive enough to have caused the magnitude of  $^{40}\text{Ar}$  loss observed. In this scenario the reheating event could have been regionally extensive, with only the most deformed samples experiencing significant  $^{40}\text{Ar}$  loss during the event. Finally, it is possible that the reheating and deformational events were spatially and temporally related. Oligocene re-burial of the eastern belt of the Niğde massif, leading to lower-

greenschist facies conditions and localized shearing along the unconformity between the metamorphic rocks and the Çamardı sediments (Umhoefer et al., 2007), may have caused the brittle deformation reflected by the pervasive thin-section scale fracturing in samples closest to the unconformity and the CAFZ. The localized heating and deformation-induced reduction in  $^{40}\text{Ar}$  retentivity would have acted together to produce the disturbed Ar systematics that characterize most of the eastern Niğde massif samples. Distinguishing between these various models will require additional detailed  $^{40}\text{Ar}/^{39}\text{Ar}$  analyses and microstructural work to better define the spatial extents of the regions affected by deformation and isotopic disturbance, and to critically evaluate the possible correlation between these processes.

The Oligocene re-heating event is recorded by T-t histories generated from two K-feldspar samples dated by  $^{40}\text{Ar}/^{39}\text{Ar}$  and modeled using the MDD model (Figs 7, 8a-d). This model exploits the occurrence of multiple scales of diffusion domains in K-feldspar to characterize diffusion over a wide range of temperatures, and has been applied to a wide range of tectonic problems (e.g. Shaw et al., 1992; Heizler and Harrison, 1998; Forster and Lister, 2010).

A fundamental premise of the MDD theory is that the diffusion of argon in laboratory outgassing experiments occurs by the same mechanisms and at the same rates as argon diffusion in nature. Formation of diffusion domains above the closure temperature for Ar in K-feldspar ( $\sim 350^\circ$ ) is also implicit in the model (Lovera et al., 1989). Other assumptions necessary for the application of the MDD model, such as those pertaining to analytical procedures and mathematical simplifications (shape and size of

diffusion domains and zero-concentration boundary conditions), are of second-order importance and do not greatly impact thermal history solutions (Lovera et al., 1991; 2002).

The results of MDD thermal models from these samples are robust. Modeling the K-feldspar thermal histories using widely different initial parameters (e.g., length of time modeled, number of iterations, temperature constraints, and maximum heating/cooling rates for the Monte Carlo and CRS pools) consistently produced T-t curves with similar geometries (Appendices 5, 6). In particular, a tightly-defined Oligocene re-heating event was common to all T-t histories despite changes in initial model parameters. Throughout MDD modeling, the initial model constraints were kept broad in order to allow the program to fully explore T-t space and avoid biasing of the results.

Absolute temperatures displayed in the T-t history results may be affected by the accuracy of activation energy (E) values calculated from the initial Arrhenius points (Figs 7c, 8c). The calculated E values for the two K-feldspar samples are low ( $43.24 \pm 3.06$  kcal/mol for 11-TR-14 and  $39.95 \pm 0.86$  kcal/mol for 11-TR-18), but fall within the range of activation energies for K-feldspar reported by Lovera et al. (1997) (mode =  $46 \pm 6$  kcal/mol). Miscalculated K-feldspar activation energies will affect the absolute temperatures in the T-t histories, but will not alter the form of the T-t curves (Lovera et al., 1997). The T-t histories will therefore still provide useful information about the massif's thermal history, although caution should be taken when considering the absolute temperature values indicated in these results.



The T-t histories generated by MDD modeling of the K-feldspar  $^{40}\text{Ar}/^{39}\text{Ar}$  results agree very well with new and previously published thermochronology results from the Niğde massif, as well as constraints imposed by structural relationships. The K-feldspar samples experienced an initial cooling from high temperatures in the Late Cretaceous, an event that is reflected by previously published  $^{40}\text{Ar}/^{39}\text{Ar}$  ages from the western belt of the massif and the high laser power steps from new muscovite  $^{40}\text{Ar}/^{39}\text{Ar}$  results. After this cooling, the K-feldspar samples experienced a period of lower temperatures. Independent field observations demonstrate that the massif was at the surface during this time, due to the deposition of partially massif-derived Paleogene Çamardı sediments directly on the metamorphic core of the massif. Although the T-t models do not tightly constrain temperatures at this time, they do not prevent the samples from being at surface conditions. Starting at ~45-35 Ma, T-t histories show that K-feldspars from the eastern margin of the massif were re-heated, reaching peak temperatures around 35-25 Ma. This re-heating event was significant enough to affect the  $^{40}\text{Ar}/^{39}\text{Ar}$  spectra from four of eight white mica samples, causing partial loss of  $^{40}\text{Ar}$ . Cooling from this re-heating is captured by new AHe results, which record ages of ~26-14 Ma (with one older exception that had an age of  $37.04 \pm 0.47$  Ma, possibly due the presence of U-rich inclusions). Although inclusions and grain morphology may have affected the accuracy and reproducibility of our AHe results, the ages agree well with the final cooling history depicted by the K-feldspar T-t histories assuming a closure temperature of ~65°C (Farley, 2002).

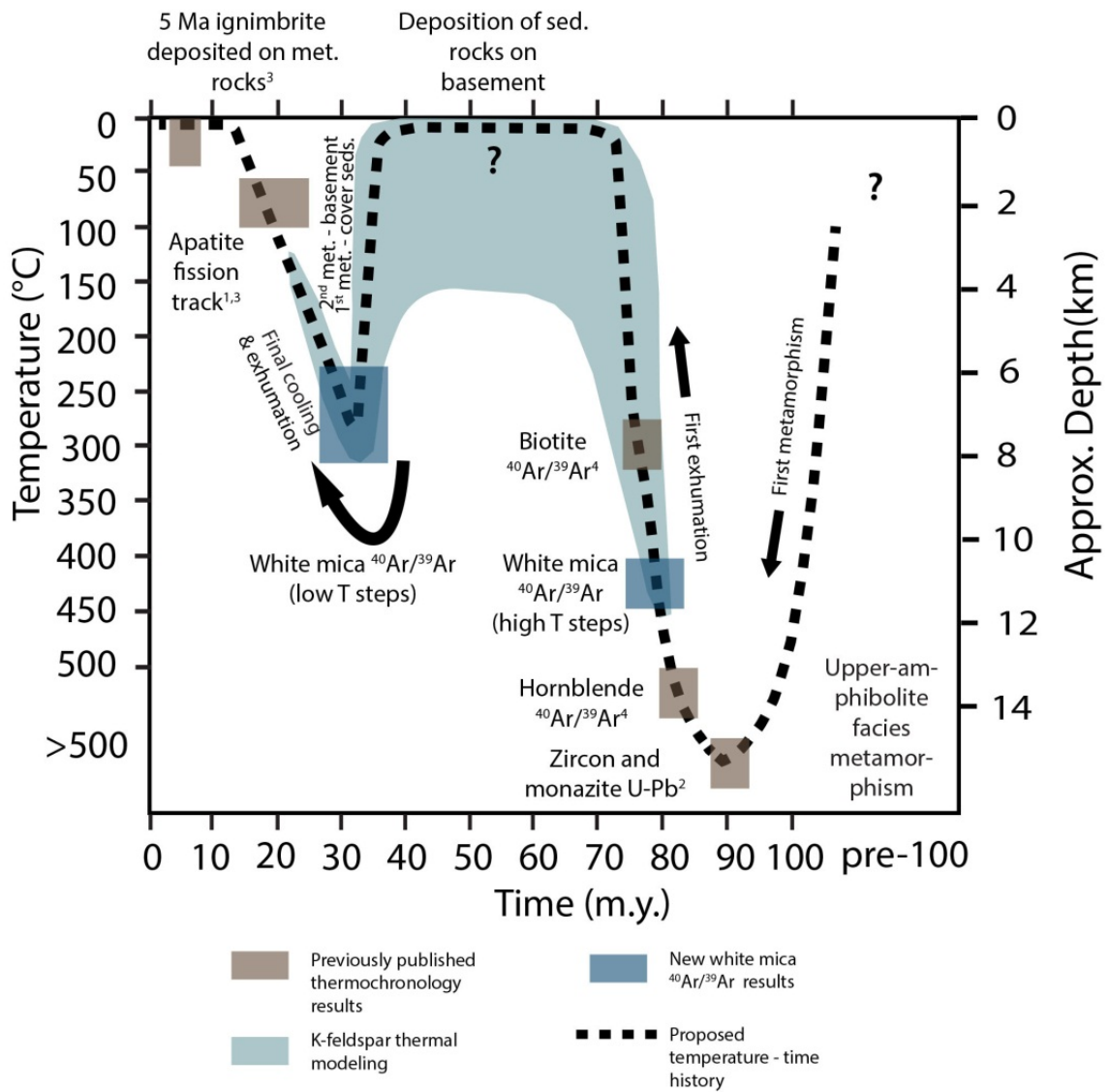


**Figure 10.** Temperature-time and depth-time histories for the Niğde Massif constructed from <sup>40</sup>Ar/<sup>39</sup>Ar muscovite and K-feldspar data (blue boxes and thermal history) and from previously published thermochronology data (taupe boxes: <sup>1</sup>Fayon et al., 2001; <sup>2</sup>Whitney et al., 2003; <sup>3</sup>Umhoefer et al., 2007; <sup>4</sup>Whitney et al., 2007). Depth-time history constructed assuming a geothermal gradient of 40°C/km, following Umhoefer et al. (2007).

## 7. Burial and Exhumation History of the Niğde Massif

The thermochronology results and key field relationships define a complete temperature-time history for the Niğde massif (Fig. 10). Thermal histories from two K-feldspar samples indicate initial cooling from peak metamorphic temperatures during the Late Cretaceous, which agrees with previously published Late Cretaceous  $^{40}\text{Ar}/^{39}\text{Ar}$  ages (~84-74 Ma) from the western belt of the Niğde massif and reflects the massif's initial exhumation (Gautier et al., 2002; 2008; Umhoefer et al., 2007; Whitney et al., 2007).

From ~60-40 Ma, sediments sourced from the massif were deposited along its eastern margin into an adjacent basin, evidence that the metamorphic rocks were exhumed to the surface by this time (Göncüoğlu et al., 1991; Yetiş et al., 1995; Gautier et al., 2002). The K-feldspar thermal histories are consistent with  $T < 150^\circ\text{C}$  during this time, since the model is unable to discern temperatures  $< \sim 150^\circ\text{C}$ . Therefore, the model results are consistent with exhumation of the rocks to (or near) the Earth's surface during this period.

The re-burial and heating of the eastern margin of the massif is captured by the K-feldspar thermal models and is also seen in the muscovite  $^{40}\text{Ar}/^{39}\text{Ar}$  results that display partial re-setting. The peak of the thermal event occurred at ~35-25 Ma. K-feldspar thermal histories show that maximum temperatures for this re-heating event were between 200 and 300°C, although these values may be rendered somewhat inaccurate by the uncertainties in the calculated activation energies. Given the occurrence of greenschist facies minerals in the Çamardı Formation and the presence of detrital muscovite with Late Cretaceous  $^{40}\text{Ar}/^{39}\text{Ar}$  ages (Umhoefer et al., 2007; Whitney et al.,

2007), temperatures were likely at least 250°C but probably not > 350°C. Utilizing a geothermal gradient of ~ 40°C/km (Umhoefer et al., 2007) and maximum re-heating temperatures of 250-350°C from K-feldspar modeling, the eastern margin of the massif was reburied to depths of 6-10 km (Fig. 10). If the geothermal gradient was closer to 25°C/km, the eastern margin of the massif would have reached depths of 10-14 km.

The AHe ages track the final exhumation and cooling of the eastern margin of the massif to ~60-70° by ~18 Ma. Structurally deeper parts of the massif cooled through the partial annealing zone of apatite (120-60°C) by ~11-12 Ma (Fayon et al., 2001). Together, the AHe ages and K-feldspar MDD models indicate a cooling rate of ~13 °C/Ma during the massif's final exhumation.

Umhoefer et al. (2007) proposed that the “yo-yo” history of the Niğde massif has been controlled by the CAFZ, which runs along the massif's eastern margin (Fig. 1). In their model, the initial metamorphism and Late Cretaceous exhumation of the massif were related to transtension and transpression cycles. Oligocene transpression triggered the re-burial of the massif and its overlying sediments, and another episode of transtension brought the entire massif and associated cover metasediments back to the surface in the Miocene. Transpression and transtension may have been related to localized steps or bends along the CAFZ and/or to regional tectonic events.

Major tectonic events took place in and near Anatolia in the Oligo-Miocene, concurrent with the massif's second burial/exhumation cycle. For example, although estimates of the age of Arabian/Eurasian collision vary, many authors place the age of the onset of collision between 30-20 Ma (Hempton, 1987; Beydoun et al., 1992; Jolivet and

Faccenna, 2000; McQuarrie et al., 2003; Allen and Armstrong, 2008; Hatzfeld and Molnar, 2010; McQuarrie and van Hinsbergen, 2013), coeval with peak re-heating in the Niğde massif (Fig. 10). If displacement on the CAFZ at this time was related to collision to the east, this may represent the earliest stages of tectonic escape in Anatolia, at least 20 million years before the inception of the North Anatolian and East Anatolian Faults.

## **8. Conclusions**

Muscovite and K-feldspar  $^{40}\text{Ar}/^{39}\text{Ar}$  and apatite (U-Th)/He thermochronology results tightly bracket the timing of a second burial and exhumation cycle experienced by the metamorphic rocks of the Niğde massif more than 30 million years after their initial cooling and exhumation to the Earth's surface. Results of this study suggest that an Oligocene tectonothermal event variably affected the muscovite K-Ar system, producing discordant age spectra in deformed samples located near the fault zone at the contact between the metamorphic rocks and the overlying Çamardı formation.  $^{40}\text{Ar}/^{39}\text{Ar}$  results for muscovite yield older (Late Cretaceous) ages and similar spectra in samples from structurally deeper levels. An Oligocene event at 35-25 Ma is also recorded in T-t histories generated from multi-diffusion domain modeling of K-feldspar  $^{40}\text{Ar}/^{39}\text{Ar}$  results from gneisses in the eastern belt. AHe results indicate cooling at  $\sim 13^\circ\text{C}/\text{Ma}$  following reburial and heating of the massif (and burial/heating of the overlying Paleogene sedimentary deposits), to  $<60\text{-}70^\circ\text{C}$  by about 18 Ma. Along with existing thermochronology ( $^{40}\text{Ar}/^{39}\text{Ar}$ , apatite fission-track) and structural data, these new results document an Oligocene event that may have been related to motion along the Central

Anatolian Fault Zone, perhaps in response to the collision of Arabia with Eurasia to the east.

## References

- Akıman, O., Erler, A., Göncüoğlu, M.C., Güleç, N., Geven, A., Türeli, T.K., and Kadioğlu, Y. K., 1993. Geochemical characteristics of granitoids along the western margin of the Central Anatolian Crystalline Complex and their tectonic implications. *Geol. J.* 28, 371-382.
- Allen, M. B. and Armstrong, H. A., 2008. Arabia-Eurasia collision and the forcing of mid-Cenozoic global cooling. *Palaeogeography, Palaeoclimatology, Palaeoecology* 265, 52-58.
- Beydoun, Z. R., Hughes Clarke, M. W., and Stoneley, R., 1992. Petroleum in the Zagros Basin: a late Tertiary foreland basin overprinted onto the outer edge of a vast hydrocarbon-rich Paleozoic-Mesozoic passive-margin shelf. In: MacQueen, R., Leckie, D. (Eds.), *Foreland Basins and Foldbelts*. AAPG Memoir, vol. 55, pp. 309-339.
- Boztuğ, D., Temiz, H., Jonckheere, R. Ratschbacher, L., 2008. Punctuated exhumation and foreland basin formation infilling in (circum)-Central Anatolia (Turkey) associated with the Neo-Tethyan closure. *Turkish J. of Earth Sci.* 17, 673-684.
- Brown, R., Beucher, R., Roper, S., Gallagher, K., Persano, C., Stuart, F., Fitzgerald, P., and Swift, D., 2011. Exploiting the natural dispersion of single crystal fragment (U-Th)/He age determinations using a new inverse approach to deriving thermal history information. Abstract V31G-06. Presented at 2011 Fall Meeting, AGU, San Francisco, Calif., 5-9 Dec.
- Cianetti, S., Gasperini, P., Boccaletti, M., and Giunchi, C., 1997. Reproducing the velocity and stress fields in the Aegean region. *Geophys. Res. Lett.* 24, no. 16, 2087-2090.
- Clark, M. and Robertson, A. H. F., 2005. Uppermost Cretaceous-Lower Tertiary Ulukışla Basin, south-central Turkey: sedimentary evolution of part of a unified basin complex within an evolving Neotethyan suture zone. *Sediment. Geol.* 173, 15-51.
- Cosca, M., Stunitz, H., Bourgeix, A-L., and Lee, J., 2011.  $^{40}\text{Ar}^*$  loss in experimentally deformed muscovite and biotite with implications for  $^{40}\text{Ar}/^{39}\text{Ar}$  geochronology of naturally deformed rocks. *Geochim. et Cosmochim. Acta* 75, 7759-7778.
- Dewey, J. F., Hempton, M. R., Kidd, W. S. F., Saroglu, F., and Şengör, A. M. C., 1986. Shortening of continental lithosphere: the neotectonics of Eastern Anatolia – a young collision zone. *Geol. Soc. London, Special Publications* 19, 1-36. Doi: 10.1144/GSL.SP.1986.019.01.01.
- Farley, K., 2002. (U-Th)/He dating: techniques, calibrations, and applications. *Reviews in Mineralogy and Geochemistry* 47, 819-844.
- Fayon, A. K., and Whitney, D. L., 2007. Interpretation of tectonic versus magmatic processes for resetting apatite fission track ages in the Niğde Massif, Turkey. *Tectonophysics* 434 (1-4), doi: 10.1016/j.tecto,2007.01.003
- Fayon, A. K., Whitney, D. L., Teyssier, C., Garver, J. I., and Dilek, Y., 2001. Effects of plate convergence obliquity on timing and mechanisms of exhumation of a midcrustal terrain, the Central Anatolian Crystalline Complex. *Earth Planet. Sci. Lett.* 92, 191-205.

- Fitzgerald, P. G., Baldwin, S. L., Webb, L. E., and O'Sullivan, P. B., 2006. Interpretation of (U-Th)/He single grain ages from slowly cooled crustal terranes: A case study from the Transantarctic Mountains of southern Victoria Land. *Chem. Geol.* 225, 91-120.
- Forster, M. A. and Lister, G. S., 2010. Argon enters the retentive zone: reassessment of diffusion parameters for K-feldspar in the South Cyclades Shear Zone, Ios, Greece. *Geol. Soc. London, Special Publications* 332, 17-34.
- Gautier, P., Bozkurt, E., Hallot, E., and Dirik, 2002. Dating the exhumation of a metamorphic dome: Geological evidence for pre-Eocene unroofing of the Niğde Massif (central Anatolia, Turkey). *Geol. Mag.* 139, 559-576.
- Gautier, P., Bozkurt, E., Bosse, V., Hallot, E., and Dirik, K., 2008. Coeval extensional shearing and lateral underflow during Late Cretaceous core complex development in the Niğde Massif, Central Anatolia, Turkey. *Tectonics* 27, TC1003, doi: 10.1029/2006TC002089.
- Göncüoğlu, M. C., Toprak, V., Kuşcu, I., Erler, A., and Olgun, E., 1991. Geology of the western part of the Central Anatolian Massif: Part 1, Southern Section. Turkish Petroleum Corporation (TPAO) Report no. 2909, 140 p.
- Hames, W. and Bowring, S., 1994. An empirical evaluation of the argon diffusion geometry in muscovite. *Earth and Planet. Sci. Lett.* 124, 161-167.
- Harrison, T. M., Célérier, J., Aikman, A. B., Hermann, J., and Heizler, M. T., 2009. Diffusion of  $^{40}\text{Ar}$  in muscovite. *Geochim. et Cosmochim. Acta* 73, 1039-1051.
- Harrison, T. M., Heizler, M. T., and Lovera, O. M., 1993. *In vacuo* crushing experiments and K-feldspar thermochronometry. *Earth Planet. Sci. Lett.* 117, 169-180.
- Hatzfeld, D. and Molnar, P., 2010. Comparisons of the kinematics and deep structures of the Zagros and Himalaya and of the Iranian and Tibetan Plateaus and geodynamic implications. *Reviews of Geophysics* 48, RG2005, doi: 10.1029/2009RG00034.
- Heizler, M. T. and Harrison, T. M. (1998) The thermal history of the New York basement determined from  $^{40}\text{Ar}/^{39}\text{Ar}$  K-feldspar studies. *J. Geophys. Res.* 103, B12, 29795-29814.
- Hempton, M. R., 1987. Constraints on Arabian plate motion and extensional history of the Red Sea. *Tectonics* 6, 687-705.
- Hourigan, J. K., Reiners, P. W., and Brandon, M. T., 2005. U-Th zonation-dependent alpha-ejection in (U-Th)/He chronometry. *Geochim. Cosmochim. Acta* 69, 3349-3365.
- Jaffey, N., and Robertson, A. H. F., 2001. New sedimentological and structural data from the Ecemiş Fault Zone, southern Turkey: Implications for its timing and offset and the Cenozoic tectonic escape of Anatolia. *J. Geol. Soc. London.* 58, 367-378.
- Jolivet, L. and Faccenna, C., 2000. Mediterranean extension and the Africa-Eurasia collision. *Tectonics* 19, 1095-1106.
- Kadıoğlu, Y. K., Dilek, Y., Güleç, N., and Foland, K., 2003. Tectonomagmatic Evolution of Bimodal Plutons in the Central Anatolian Crystalline Complex, Turkey. *J. of Geol.* 111, 671-690.



- Kirschner, D., Cosca, M., Masson, H., and Hunziker, J., 1996. Staircase  $^{40}\text{Ar}/^{39}\text{Ar}$  spectra of fine-grained white mica: Timing and duration of deformation and empirical constraints on argon diffusion. *Geology* 24, 747-750.
- Koçyiğit, A. and Beyhan, A., 1998. A new intracontinental transcurrent structure: The Central Anatolian Fault Zone, Turkey. *Tectonophysics*, 284, 317-336.
- Kramar, N., Cosca, M. A., Huziker, J. C., 2001. Heterogeneous  $^{40}\text{Ar}$  distributions in naturally deformed muscovite: in situ UV-laser ablation evidence for microstructurally controlled intragrain diffusion. *Earth Planet. Sci. Lett.* 192, 377-388.
- Kuiper, K. F., Deino, A., Hilgen, F. J., Krijgsman, W., Renne, P. R. and Wijbrans, J. R., 2008. Synchronizing Rock Clocks of Earth History. *Science* 25, 500-504. Doi: 10.1126/science.1154339
- Kula, J., Spell, T. L., and Zanetti, K. A., 2010.  $^{40}\text{Ar}/^{39}\text{Ar}$  analyses of artificially mixed micas and the treatment of complex age spectra from samples with multiple mica populations. *Chem. Geol.* 275, 67-77.
- Le Pichon, X., Chamot-Rooke, N., Lallemand, S., Noomen, R., and Veis, G., 1995. Geodetic determination of the kinematics of central Greece with respect to Europe: Implications for eastern Mediterranean tectonics. *J. Geophys. Res.* 100, 12675-12690.
- Lovera, O. M., Grove, M., and Harrison, T. M., 2002. Systematic analysis of K-feldspar  $^{40}\text{Ar}/^{39}\text{Ar}$  step-heating experiments II: relevance of laboratory K-feldspar argon diffusion properties to Nature. *Geochim. Cosmochim. Acta* 66, 1237-1255.
- Lovera, O. M., Grove, M., Harrison, T. M., and Maon, K. I., 1997. Systematic analysis of K-feldspar  $^{40}\text{Ar}/^{39}\text{Ar}$  step heating results: 1. Significance of activation energy determinations. *Geochem. Cosmochim. Acta* 61, 3171-3192.
- Lovera, O. M., Richter, F. M., and Harrison, T. M., 1989. The  $^{40}\text{Ar}/^{39}\text{Ar}$  thermochronometry for slowly cooled samples having a distribution of diffusion domain sizes. *J. Geophys. Research* 94, 17917-17935.
- Lovera, O. M., Richter, F. M., and Harrison, T. M., 1991. Diffusion domains determined by  $^{39}\text{Ar}$  release during step heating. *J. Geophys. Res.* 96, 2057-2069.
- Lundgren, P., Giardini, D., and Russo, R. M., 1998. A geodynamic framework for eastern Mediterranean kinematics. *Geophys. Res. Lett.* 25, 4007-4010.
- McDougall, I. and Harrison, T. M., 1999. *Geochronology and Thermochronology by the  $^{40}\text{Ar}/^{39}\text{Ar}$  Method*, Second ed. Oxford University Press. 269 pp.
- McKenzie, D., 1976. The East Anatolian Fault: A major structure in Eastern Turkey. *Earth Planet Sci. Lett.* 29, 189-193.
- McQuarrie, N. and van Hinsbergen, J. J., 2013. Retrodeforming the Arabia-Eurasia collision zone: Age of collision versus magnitude of continental subduction. *Geology* 41, 315-318.
- McQuarrie, N., Stock, J. M., Verdel, C., and Wernicke, B. P., 2003. Cenozoic evolution of Neotethys and implications for the causes of plate motions. *Geophys. Res. Lett.* 30, 2036, doi: 10.1029/2003GL017992.
- Molnar, P., 1992. Brace-Goetze strength-profiles, the partitioning of strike-slip and thrust faulting at zones of oblique convergence, and the stress-heat paradox of the San

- Andreas fault, in: Evans, B. and Wong, T.-F. (Eds.), *Fault Mechanics and Transport properties of Rocks*. Academic, San Diego, California, pp. 435-459.
- Okay, A.I., and Tüysüz, O., 1999. Tethyan sutures of northern Turkey. In: *The Mediterranean Basin; Tertiary Extension within the Alpine Orogeny*, Vol. 156, pp. 475-515, Geological Society Special Publications.
- Okay, A. I., Tüysüz, O, and Kaya, Ş., 2004. From transpression to transtension: changes in morphology and structure around a bend on the North Anatolian Fault in the Marmara region. *Tectonophysics* 391, 259-282.
- Renne, P. R., Swisher, C. C., Deino, A. L., Karner, D. B., Owens, T. L., and DePaolo, D. J., 1998. Intercalibration of standards, absolute ages and uncertainties in  $^{40}\text{Ar}/^{39}\text{Ar}$  dating. *Chem. Geol.* 145, 117-152.
- Robertson, A.H.F., and Dixon, J.E., 1984. Introduction: aspects of the geological evolution of the eastern Mediterranean. In: Dixon, J.E., and Robertson, A.H.F. (Eds.), *The Geological Evolution of the Eastern Mediterranean*. Geol. Soc., London, Spec. Publ. 17, p. 1-74.
- Şengör, A. M. and Natal'in, B. A., 1996. Turcic-type orogeny and its role in the making of the continental crust. *Annu. Rev. Earth Planet. Sci.* 24, 263-337.
- Şengör, A. M. C., and Yılmaz, Y., 1981. Tethyan evolution of Turkey: A plate tectonic approach. *Tectonophysics* 75, 181-241.
- Shaw, R. E., Zeitler, P. K., McDougal, I., and Tingate, P. R., 1992. The Palaeozoic history of an unusual intracratonic thrust belt in central Australia based on  $^{40}\text{Ar}$ - $^{39}\text{Ar}$ , K-Ar and fission track dating. *J. Geophys. Soc. London* 149, 937-954.
- Spotila, J. A., Niemi, N., Brady, R., House, M., Buscher, J., and Oskin, M., 2007. Long-term continental deformation associated with transpressive plate motion: The San Andreas fault. *Geology* 35, 967-970, doi: 10.1130/G23816A.1.
- Teyssier, C., Tikoff, B., and Markley, B., 1995. Oblique plate motion and continental tectonics. *Geology* 23, 447-450.
- Umhoefer, P. J., Whitney, D. L., Teyssier, C., Fayon, A. K. Casale, G., and Heizler, M. J., 2007. Yo-yo tectonics in a wrench zone, in: Till, A. B. et al. (Eds.), *Exhumation Associated With Continental Strike-Slip Systems*. Spec. Pap. Geol. Soc. Am. 434, doi: 10.1130/2007.2343(03).
- West, D. and Lux, R., 1993. Dating mylonitic deformation by the  $^{40}\text{Ar}$ - $^{39}\text{Ar}$  method: An example from the Norumbega Fault Zone, Maine. *Earth. Planet. Sci. Lett.* 120, 221-237.
- Whitney D. L., Teyssier, C., Dilek, Y., and Fayon, A. K., 2001. Metamorphism of the Central Anatolian Crystalline Complex, Turkey: Influence of orogen-normal collision vs. wrench dominated tectonics on P-T-t paths. *J. Met. Geol.* 19, 411-432.
- Whitney, D. L. and Hamilton, M. A., 2004. Timing of high-grade metamorphism in central Turkey and the assembly of Anatolia. *J. Geol. Soc. London* 161, 823-828.
- Whitney, D. L., and Dilek, Y., 1997. Core complex development in central Anatolia. *Geology* 25, 1023-1026.

- Whitney, D. L., and Dilek, Y., 1998. Metamorphism during crustal thickening and extension in central Anatolia: the Niğde metamorphic core complex. *J. Petrol.* 39, 1385-1403.
- Whitney, D. L., Teyssier, C., and Heizler, M. T., 2007. Gneiss domes, metamorphic core complexes, and wrench zones: Thermal and structural evolution of the Niğde massif, central Anatolia. *Tectonics* 26, TC5002, doi: 10.1029/2006TC002040.
- Whitney, D. L., Teyssier, C., Fayon, A. K., Hamilton, M. A., and Heizler, M. J., 2003. Tectonic controls on metamorphism, partial melting, and intrusion: Timing of regional metamorphism and magmatism of the Niğde Massif, Turkey. *Tectonophysics* 376, 37-60.
- Whitney, D. L., Umhoefer, P. J., Teyssier, C., and Fayon, A. K., 2008. Yo-yo tectonics of the Niğde massif during wrenching in central Anatolia. *Turkish J. of Earth Sci.* 17, 209-217.
- Yetiş, C., Kelling, G., Gökçen, S.L., and Baroz, F., 1995. A revised stratigraphic framework for Later Cenozoic sequences in the northeastern Mediterranean region. *Geologisches Rundschau* 84, 794-812, doi: 10.1007/s005310050041

## Appendix 1. Sample information

<u>Sample Name</u>	<u>Zone</u>	<u>Northing</u>	<u>Easting</u>	<u>Rock Type</u>	<u>Location Notes</u>	<u>Analyses</u>
11-TR-02	36	671616	4188636	Gneiss	Kavaklıgöl	Muscovite $^{40}\text{Ar}/^{39}\text{Ar}$
11-TR-03	36	671477	4188480	Gneiss	Kavaklıgöl	Muscovite $^{40}\text{Ar}/^{39}\text{Ar}$
11-TR-04	36	671577	4188376	Cataclasite/gneiss	Kavaklıgöl	Muscovite $^{40}\text{Ar}/^{39}\text{Ar}$
11-TR-05	36	672020	4188509	Brecciated gneiss	Kavaklıgöl	Muscovite $^{40}\text{Ar}/^{39}\text{Ar}$
11-TR-14	36	674000	4190139	Gneiss	Çamardı-Üçkapılı	Musc., Kfs $^{40}\text{Ar}/^{39}\text{Ar}$
11-TR-16	36	671847	4192558	Quartzite	Çamardı-Üçkapılı	Muscovite $^{40}\text{Ar}/^{39}\text{Ar}$
11-TR-17	36	671910	4192493	Leucogneiss	Çamardı-Üçkapılı	Muscovite $^{40}\text{Ar}/^{39}\text{Ar}$
11-TR-18	36	671878	4192490	Leucogneiss	Çamardı-Üçkapılı	Musc., Kfs $^{40}\text{Ar}/^{39}\text{Ar}$
11-CAT-04	36	672065	4188521	Foliated sandstone	Kavaklıgöl	Apatite (U-Th)/He
11-CAT-06	36	675661	4193389	Coarse sandstone	Evliya Tepe	Apatite (U-Th)/He
11-CAT-07	36	675617	4192789	Sandstone	Evliya Tepe	Apatite (U-Th)/He
11-CAT-12	36	674203	4189726	Sandstone	Çamardı	Apatite (U-Th)/He
11-CAT-15	36	665210	4184699	Green sandstone	S Niğde	Apatite (U-Th)/He
11-CAT-16	36	663062	4184425	Sandstone	S Niğde	Apatite (U-Th)/He
12-CAT-4D	36	677117	4198860	Quartz-schist	Niğde/Eynelli	Apatite (U-Th)/He
12-CAT-7	36	675585	4193432	Schist	Niğde/Evliya Tepe	Apatite (U-Th)/He
12-CAT-8A	36	672727	4194784	Quartzite	Niğde	Apatite (U-Th)/He
12-CAT-10A	36	674447	4194482	Quartz-schist	Niğde	Apatite (U-Th)/He
12-CAT-11B	36	675111	4192262	Cataclasite	Niğde	Apatite (U-Th)/He
ND98-3	36	656888	4205132	Gneiss	NW Niğde	Apatite (U-Th)/He
ND01-5	36	626991	4150345	Granite	SE Niğde	Apatite (U-Th)/He

**Appendix 2. Electron microprobe analyses of muscovite  $^{40}\text{Ar}/^{39}\text{Ar}$  samples**

	<u>11-TR- 03</u>	<u>11-TR- 04</u>	<u>11-TR- 05</u>	<u>11-TR- 14</u>	<u>11-TR- 18</u>
<b>SiO<sub>2</sub></b>	45.63	46.46	45.02	45.06	44.74
<b>TiO<sub>2</sub></b>	0.29	0.00	0.08	0.27	0.08
<b>Al<sub>2</sub>O<sub>3</sub></b>	37.73	38.47	37.60	37.29	36.31
<b>FeO</b>	1.28	0.92	1.05	0.81	1.80
<b>MnO</b>	0.10	0.07	0.05	0.02	0.06
<b>MgO</b>	0.34	0.49	0.83	0.62	0.55
<b>CaO</b>	0.03	0.00	0.05	0.06	0.03
<b>Na<sub>2</sub>O</b>	0.82	0.57	0.64	0.49	0.36
<b>K<sub>2</sub>O</b>	10.18	12.09	11.37	11.67	11.38
<b>Total</b>	96.40	99.08	96.69	96.30	95.30
Cations calculated on 11 oxygen basis					
<b>Si</b>	3.00	2.99	2.97	2.98	3.00
<b>Al<sup>IV</sup></b>	1.00	1.01	1.03	1.02	1.00
<b>Al<sup>VI</sup></b>	5.57	5.55	5.55	5.52	5.44
<b>Ti</b>	0.01	0.00	0.00	0.01	0.00
<b>FeO</b>	0.07	0.07	0.05	0.07	0.10
<b>Mn</b>	0.01	0.00	0.00	0.00	0.00
<b>Mg</b>	0.03	0.02	0.02	0.03	0.06
<b>Ca</b>	0.00	0.00	4.11	0.00	0.00
<b>Na</b>	0.10	0.07	0.08	0.06	0.05
<b>K</b>	0.85	0.99	0.96	0.99	0.97

### Appendix 3. Muscovite $^{40}\text{Ar}/^{39}\text{Ar}$ results

Watts	Relative Isotopic Abundances										Derived Results						
	$^{40}\text{Ar}$	$\pm 1\sigma$	$^{39}\text{Ar}$	$\pm 1\sigma$	$^{38}\text{Ar}$	$\pm 1\sigma$	$^{37}\text{Ar}$	$\pm 1\sigma$	$^{36}\text{Ar}$	$\pm 1\sigma$	$^{39}\text{Ar}$ (Mol x $10^{-14}$ )	$^{39}\text{Ar}$ % of total	Ca/K	$\pm 1\sigma$	% $^{40}\text{Ar}^a$	Age (Ma)	$\pm 1\sigma$
<b>11-TR-02 - muscovite</b>																	
<b><math>J \pm 1\sigma = 6.63 \times 10^{-4} \pm 1.3 \times 10^{-6}</math></b>																	
0.10	16.8764	0.0168	0.3085	0.0025	0.0050	0.0009	0.0024	0.0019	0.0074	0.0006	0.68	1.8	0.015	0.012	87.0	56.101	0.83
0.15	179.6039	0.1301	2.6064	0.0054	0.0363	0.0010	0.0399	0.0015	0.0201	0.0007	5.76	15.0	0.030	0.001	96.7	78.041	0.20
0.20	137.9380	0.0862	1.9367	0.0045	0.0287	0.0009	0.0397	0.0015	0.0201	0.0007	4.28	11.2	0.040	0.002	95.7	79.791	0.23
0.25	226.1972	0.1501	3.1897	0.0066	0.0465	0.0010	0.0716	0.0025	0.0209	0.0007	7.05	18.4	0.044	0.002	97.3	80.729	0.20
0.30	163.0639	0.1801	2.3110	0.0045	0.0312	0.0010	0.1171	0.0017	0.0117	0.0007	5.11	13.3	0.099	0.001	97.9	80.831	0.21
0.35	154.6452	0.1301	2.1801	0.0056	0.0284	0.0011	0.0589	0.0022	0.0104	0.0007	4.82	12.6	0.053	0.002	98.0	81.351	0.25
0.40	74.0933	0.1201	1.0355	0.0038	0.0097	0.0009	0.0259	0.0014	0.0023	0.0008	2.29	6.0	0.049	0.003	99.1	82.933	0.42
0.50	68.2716	0.0572	0.9463	0.0035	0.0111	0.0010	0.0086	0.0015	0.0061	0.0006	2.09	5.5	0.018	0.003	97.4	82.161	0.38
0.60	57.4159	0.0513	0.7988	0.0035	0.0085	0.0010	0.0000	0.0014	0.0011	0.0006	1.77	4.6	0.000	0.003	99.5	83.585	0.46
0.70	42.6678	0.0453	0.5908	0.0031	0.0081	0.0009	0.1155	0.0028	0.0021	0.0006	1.31	3.4	0.383	0.010	98.5	83.228	0.56
0.80	28.2820	0.0295	0.3841	0.0028	0.0021	0.0010	0.0001	0.0014	0.0001	0.0006	0.85	2.2	0.000	0.007	99.9	85.939	0.84
0.90	17.5910	0.0158	0.2358	0.0030	0.0035	0.0009	0.0000	0.0015	0.0002	0.0006	0.52	1.4	0.000	0.012	99.6	86.843	1.40
1.00	20.5932	0.0314	0.2824	0.0023	0.0039	0.0009	0.0000	0.0014	0.0002	0.0006	0.62	1.6	0.000	0.010	99.7	84.990	1.05
1.20	37.8635	0.0433	0.5125	0.0026	0.0078	0.0009	0.0000	0.0021	0.0018	0.0006	1.13	3.0	0.000	0.008	98.6	85.132	0.60
<b>11-TR-04 - muscovite</b>																	
<b><math>J \pm 1\sigma = 6.63 \times 10^{-4} \pm 1.3 \times 10^{-6}</math></b>																	
0.10	27.5611	0.0334	0.5478	0.0032	0.0142	0.0010	0.0775	0.0017	0.0436	0.0007	1.21	3.0	0.277	0.006	53.2	31.777	0.52
0.15	65.0361	0.0503	0.9959	0.0034	0.0328	0.0010	0.0545	0.0021	0.1044	0.0008	2.20	5.5	0.107	0.004	52.6	40.621	0.34
0.20	163.1313	0.1002	1.8419	0.0044	0.0689	0.0011	0.1332	0.0018	0.2428	0.0010	4.07	10.2	0.142	0.002	56.0	58.428	0.31
0.25	194.4494	0.2201	1.7754	0.0049	0.0882	0.0011	0.0914	0.0017	0.3498	0.0013	3.92	9.8	0.101	0.002	46.8	60.377	0.40
0.30	208.4768	0.2201	1.5616	0.0041	0.0970	0.0013	0.0510	0.0017	0.4052	0.0013	3.45	8.6	0.064	0.002	42.6	66.767	0.46
0.35	175.6589	0.0952	1.2806	0.0041	0.0785	0.0012	0.0444	0.0016	0.3459	0.0012	2.83	7.1	0.068	0.002	41.8	67.362	0.49
0.40	140.2512	0.0842	1.4483	0.0051	0.0532	0.0012	0.0215	0.0016	0.1777	0.0009	3.20	8.0	0.029	0.002	62.6	71.094	0.39
0.50	112.9832	0.1901	1.3864	0.0043	0.0367	0.0011	0.0280	0.0017	0.0974	0.0008	3.06	7.7	0.040	0.002	74.5	71.267	0.38
0.60	94.3213	0.0702	1.1775	0.0039	0.0277	0.0010	0.0158	0.0017	0.0767	0.0008	2.60	6.5	0.026	0.003	76.0	71.394	0.38

0.70	145.5064	0.1101	1.9453	0.0051	0.0429	0.0010	0.0126	0.0015	0.0962	0.0008	4.30	10.8	0.013	0.001	80.5	70.629	0.28
0.80	104.5588	0.0792	1.2774	0.0042	0.0334	0.0011	0.0087	0.0015	0.0773	0.0007	2.82	7.1	0.013	0.002	78.2	74.987	0.36
0.90	68.4640	0.0632	0.9144	0.0035	0.0179	0.0010	0.0084	0.0015	0.0357	0.0007	2.02	5.1	0.018	0.003	84.6	74.243	0.43
1.00	56.8471	0.0553	0.7796	0.0031	0.0149	0.0011	0.0018	0.0023	0.0251	0.0006	1.72	4.3	0.005	0.006	87.0	74.340	0.44
1.20	24.9855	0.0563	0.2307	0.0051	0.0098	0.0010	0.0000	0.0022	0.0317	0.0007	0.51	1.3	0.000	0.019	62.5	79.233	2.03
1.50	22.4322	0.0394	0.2431	0.0026	0.0061	0.0009	0.0000	0.0015	0.0153	0.0006	0.54	1.3	0.000	0.012	79.9	86.157	1.28
2.00	37.8657	0.0483	0.4543	0.0046	0.0111	0.0010	0.0083	0.0015	0.0183	0.0006	1.00	2.5	0.036	0.007	85.7	83.526	0.98
4.00	16.2691	0.0141	0.2006	0.0021	0.0040	0.0009	0.0046	0.0015	0.0073	0.0006	0.44	1.1	0.045	0.015	86.8	82.371	1.32

**11-TR-05 - muscovite**

$$J \pm 1\sigma = 6.63 \times 10^{-4} \pm 1.3 \times 10^{-6}$$

0.10	19.9512	0.0932	0.7356	0.0034	0.0090	0.0010	0.1249	0.0018	0.0066	0.0006	1.62	3.1	0.333	0.005	90.2	29.054	0.36
0.15	41.3034	0.0523	1.2460	0.0044	0.0179	0.0011	0.2100	0.0021	0.0065	0.0006	2.75	5.2	0.330	0.004	95.4	37.449	0.24
0.20	102.8522	0.0842	2.9806	0.0068	0.0387	0.0011	0.2458	0.0020	0.0194	0.0007	6.58	12.5	0.162	0.001	94.4	38.591	0.15
0.25	67.2202	0.0622	2.0095	0.0044	0.0295	0.0009	0.3626	0.0020	0.0159	0.0007	4.44	8.4	0.354	0.002	93.1	36.877	0.16
0.30	68.5707	0.0702	1.9857	0.0043	0.0258	0.0009	0.1440	0.0018	0.0100	0.0006	4.39	8.3	0.142	0.002	95.7	39.127	0.17
0.35	48.9485	0.0473	1.3478	0.0044	0.0151	0.0009	0.0287	0.0015	0.0052	0.0006	2.98	5.6	0.042	0.002	96.8	41.614	0.23
0.40	68.3994	0.0672	1.8262	0.0053	0.0207	0.0010	0.0174	0.0015	0.0109	0.0006	4.03	7.7	0.019	0.002	95.3	42.219	0.20
0.50	40.6572	0.0473	1.0767	0.0038	0.0146	0.0010	0.0308	0.0016	0.0078	0.0006	2.38	4.5	0.056	0.003	94.3	42.142	0.27
0.60	54.3922	0.0523	1.3449	0.0048	0.0206	0.0011	0.0156	0.0014	0.0117	0.0006	2.97	5.6	0.023	0.002	93.7	44.773	0.25
0.70	80.0034	0.0573	1.8111	0.0055	0.0249	0.0011	0.0165	0.0014	0.0142	0.0007	4.00	7.6	0.018	0.002	94.8	49.421	0.23
0.80	93.3140	0.0662	2.0323	0.0051	0.0245	0.0011	0.0212	0.0015	0.0118	0.0007	4.49	8.5	0.020	0.001	96.3	52.140	0.21
0.90	58.5500	0.1101	1.2717	0.0043	0.0180	0.0009	0.0223	0.0015	0.0093	0.0007	2.81	5.3	0.034	0.002	95.3	51.764	0.30
1.00	74.7459	0.0962	1.4171	0.0083	0.0190	0.0010	0.0180	0.0015	0.0086	0.0007	3.13	5.9	0.025	0.002	96.6	59.975	0.42
1.20	76.8081	0.0722	1.5024	0.0050	0.0167	0.0009	0.0198	0.0015	0.0067	0.0006	3.32	6.3	0.026	0.002	97.4	58.648	0.28
1.50	32.1393	0.0374	0.6563	0.0029	0.0089	0.0010	0.0613	0.0016	0.0054	0.0006	1.45	2.8	0.183	0.005	95.0	54.858	0.42
2.00	32.3561	0.0503	0.5549	0.0034	0.0064	0.0010	0.0167	0.0014	0.0023	0.0006	1.23	2.3	0.059	0.005	97.9	67.079	0.59
4.00	4.3549	0.0141	0.0617	0.0018	0.0010	0.0010	0.0036	0.0014	0.0006	0.0006	0.14	0.3	0.115	0.046	96.2	79.467	4.19

**11-TR-14 - muscovite**

$$J \pm 1\sigma = 6.63 \times 10^{-4} \pm 1.3 \times 10^{-6}$$

0.10	11.3528	0.0138	0.3042	0.0022	0.0111	0.0009	0.0556	0.0015	0.0169	0.0006	0.67	2.3	0.358	0.010	56.2	24.926	0.74
0.15	16.8999	0.0202	0.4247	0.0026	0.0073	0.0010	0.0618	0.0017	0.0158	0.0007	0.94	3.2	0.285	0.008	72.4	34.178	0.62

0.20	40.3567	0.0544	1.0031	0.0038	0.0174	0.0010	0.0759	0.0017	0.0168	0.0007	2.22	7.6	0.148	0.003	87.8	41.768	0.30
0.25	36.9393	0.0455	0.8610	0.0051	0.0120	0.0010	0.0448	0.0018	0.0088	0.0007	1.90	6.6	0.102	0.004	92.9	47.110	0.41
0.30	41.4349	0.0634	0.9195	0.0038	0.0107	0.0009	0.0415	0.0017	0.0096	0.0007	2.03	7.0	0.088	0.004	93.2	49.560	0.35
0.35	27.4010	0.0495	0.6000	0.0032	0.0102	0.0010	0.0235	0.0015	0.0070	0.0006	1.32	4.6	0.077	0.005	92.5	49.869	0.48
0.40	34.4933	0.0554	0.7680	0.0035	0.0075	0.0009	0.0269	0.0016	0.0061	0.0007	1.70	5.9	0.069	0.004	94.8	50.251	0.40
0.50	28.7821	0.0416	0.6251	0.0035	0.0111	0.0010	0.0254	0.0017	0.0069	0.0006	1.38	4.8	0.080	0.005	93.0	50.512	0.47
0.60	25.6763	0.0396	0.5418	0.0035	0.0064	0.0009	0.0194	0.0015	0.0055	0.0006	1.20	4.1	0.070	0.006	93.7	52.375	0.54
0.70	48.2179	0.0475	1.0303	0.0036	0.0109	0.0010	0.0607	0.0017	0.0084	0.0007	2.28	7.9	0.115	0.003	94.9	52.374	0.31
0.80	42.2587	0.0594	0.8357	0.0060	0.0107	0.0009	0.0464	0.0017	0.0098	0.0007	1.85	6.4	0.109	0.004	93.2	55.523	0.50
0.90	35.7500	0.0664	0.7029	0.0037	0.0106	0.0009	0.0728	0.0018	0.0072	0.0007	1.55	5.4	0.203	0.005	94.1	56.385	0.47
1.00	33.5890	0.0564	0.6228	0.0034	0.0079	0.0010	0.0814	0.0020	0.0039	0.0007	1.38	4.7	0.256	0.006	96.6	61.281	0.53
1.20	41.4303	0.0495	0.7461	0.0026	0.0081	0.0009	0.0447	0.0017	0.0047	0.0007	1.65	5.7	0.117	0.004	96.7	63.118	0.40
1.50	61.5570	0.0594	1.1152	0.0035	0.0141	0.0010	0.1540	0.0018	0.0083	0.0006	2.46	8.5	0.271	0.003	96.0	62.362	0.31
2.00	80.8573	0.0664	1.4043	0.0041	0.0184	0.0011	0.4088	0.0024	0.0115	0.0006	3.10	10.7	0.571	0.004	95.8	64.861	0.28
4.00	41.4990	0.0594	0.6197	0.0030	0.0093	0.0009	0.2882	0.0034	0.0046	0.0006	1.37	4.7	0.912	0.012	96.8	75.976	0.54

#### 11-TR-16 - muscovite

$$J \pm 1\sigma = 6.63e^{-4} \pm 1.3e^{-6}$$

0.10	57.8953	0.0814	0.9539	0.0033	0.0185	0.0009	0.0039	0.0015	0.0240	0.0007	2.11	3.1	0.008	0.003	87.7	62.642	0.36
0.15	163.5184	0.1203	2.5284	0.0067	0.0363	0.0010	0.0004	0.0015	0.0214	0.0007	5.58	8.2	0.000	0.001	96.1	72.914	0.27
0.20	281.3327	0.2002	4.2518	0.0101	0.0625	0.0012	0.0042	0.0016	0.0332	0.0007	9.39	13.7	0.002	0.001	96.5	74.858	0.25
0.25	211.2254	0.1203	3.2159	0.0270	0.0407	0.0015	0.0063	0.0015	0.0166	0.0007	7.10	10.4	0.004	0.001	97.7	75.195	0.65
0.30	211.1532	0.2002	3.2037	0.0073	0.0437	0.0011	0.0021	0.0021	0.0109	0.0007	7.08	10.4	0.001	0.001	98.5	76.047	0.25
0.35	165.1076	0.1203	2.4998	0.0069	0.0322	0.0012	0.0003	0.0014	0.0082	0.0007	5.52	8.1	0.000	0.001	98.5	76.251	0.28
0.40	156.0781	0.1702	2.3493	0.0062	0.0317	0.0010	0.0005	0.0015	0.0117	0.0007	5.19	7.6	0.000	0.001	97.8	76.122	0.28
0.50	124.3908	0.1302	1.8715	0.0089	0.0264	0.0010	0.0008	0.0015	0.0095	0.0007	4.14	6.0	0.001	0.002	97.8	76.130	0.42
0.60	120.3077	0.0844	1.8138	0.0050	0.0220	0.0009	0.0000	0.0021	0.0071	0.0008	4.01	5.9	0.000	0.002	98.2	76.354	0.30
0.70	141.2495	0.1702	2.1352	0.0046	0.0331	0.0010	0.0078	0.0014	0.0146	0.0007	4.72	6.9	0.007	0.001	97.0	75.175	0.27
0.80	140.4564	0.1203	2.1568	0.0074	0.0281	0.0011	0.0000	0.0020	0.0052	0.0007	4.76	7.0	0.000	0.002	98.9	75.486	0.32
0.90	99.4510	0.1003	1.5436	0.0052	0.0221	0.0011	0.0000	0.0022	0.0075	0.0007	3.41	5.0	0.000	0.003	97.8	73.868	0.33
1.00	38.4133	0.0526	0.6358	0.0029	0.0076	0.0010	0.0000	0.0015	0.0017	0.0006	1.40	2.1	0.000	0.005	98.7	69.971	0.49
1.20	40.9468	0.0427	0.6919	0.0037	0.0099	0.0010	0.0005	0.0015	0.0030	0.0006	1.53	2.2	0.001	0.004	97.8	67.977	0.50
1.50	19.7417	0.0516	0.3153	0.0025	0.0055	0.0009	0.0015	0.0023	0.0013	0.0006	0.70	1.0	0.009	0.014	98.0	72.006	0.91
2.00	23.0117	0.0923	0.3734	0.0028	0.0062	0.0010	0.0003	0.0014	0.0020	0.0006	0.82	1.2	0.002	0.008	97.4	70.469	0.83



4.00	26.7388	0.0447	0.4099	0.0031	0.0092	0.0010	0.0001	0.0016	0.0018	0.0006	0.91	1.3	0.001	0.008	98.0	74.937	0.80
------	---------	--------	--------	--------	--------	--------	--------	--------	--------	--------	------	-----	-------	-------	------	--------	------

**11-TR-17 - muscovite**

$J \pm 1\sigma = 6.63e^{-4} \pm 1.3e^{-6}$

0.10	81.7348	0.0972	1.2830	0.0043	0.0216	0.0010	0.0655	0.0021	0.0252	0.0007	2.83	2.9	0.100	0.003	90.9	68.011	0.33
0.15	123.3018	0.0693	2.2603	0.0050	0.0317	0.0012	0.0587	0.0021	0.0160	0.0007	4.99	5.1	0.051	0.002	96.2	61.724	0.22
0.20	235.2808	0.1901	3.9973	0.0083	0.0503	0.0012	0.0676	0.0021	0.0152	0.0007	8.83	8.9	0.033	0.001	98.1	67.817	0.21
0.25	127.6646	0.1002	2.1190	0.0055	0.0257	0.0011	0.0225	0.0022	0.0052	0.0006	4.68	4.7	0.021	0.002	98.8	69.872	0.25
0.30	180.0225	0.1501	2.9075	0.0069	0.0383	0.0011	0.0203	0.0021	0.0074	0.0007	6.42	6.5	0.014	0.001	98.8	71.759	0.24
0.35	125.3724	0.0892	2.0179	0.0060	0.0262	0.0010	0.0163	0.0021	0.0064	0.0008	4.46	4.5	0.016	0.002	98.5	71.797	0.29
0.40	133.6756	0.1901	2.1499	0.0160	0.0292	0.0010	0.0174	0.0020	0.0052	0.0007	4.75	4.8	0.016	0.002	98.8	72.100	0.57
0.50	120.3141	0.1202	1.9518	0.0054	0.0247	0.0010	0.0160	0.0021	0.0064	0.0006	4.31	4.4	0.016	0.002	98.4	71.202	0.28
0.60	117.8624	0.0862	1.9184	0.0075	0.0226	0.0010	0.0102	0.0024	0.0027	0.0006	4.24	4.3	0.010	0.003	99.3	71.599	0.34
0.70	171.1457	0.1401	2.7330	0.0150	0.0432	0.0010	0.0305	0.0021	0.0088	0.0006	6.04	6.1	0.022	0.001	98.5	72.336	0.43
0.80	205.9749	0.1801	3.3363	0.0070	0.0423	0.0011	0.0341	0.0022	0.0069	0.0006	7.37	7.5	0.020	0.001	99.0	71.713	0.23
0.90	204.1240	0.1301	3.2797	0.0100	0.0436	0.0011	0.0434	0.0021	0.0088	0.0007	7.25	7.3	0.026	0.001	98.7	72.082	0.28
1.00	188.2365	0.1202	3.0057	0.0064	0.0411	0.0010	0.0349	0.0022	0.0086	0.0007	6.64	6.7	0.023	0.001	98.7	72.470	0.23
1.20	225.3503	0.1501	3.6442	0.0079	0.0499	0.0011	0.0419	0.0021	0.0094	0.0007	8.05	8.2	0.023	0.001	98.8	71.661	0.23
1.50	332.4431	0.2201	5.6440	0.0096	0.0765	0.0012	0.0811	0.0022	0.0206	0.0008	12.47	12.6	0.028	0.001	98.2	67.911	0.19
2.00	130.3665	0.0882	1.9797	0.0051	0.0270	0.0010	0.0275	0.0022	0.0077	0.0007	4.37	4.4	0.027	0.002	98.3	75.830	0.28
4.00	33.2367	0.0693	0.4854	0.0026	0.0061	0.0009	0.0075	0.0020	0.0012	0.0006	1.07	1.1	0.030	0.008	99.0	79.337	0.64

**11-TR-18 - muscovite**

$J \pm 1\sigma = 6.63x 10^{-4} \pm 1.3 x 10^{-6}$

0.10	20.0249	0.0316	0.2145	0.0027	0.0091	0.0009	0.0038	0.0015	0.0268	0.0006	0.47	0.3	0.035	0.014	60.5	66.358	1.32
0.15	46.7549	0.0513	0.3892	0.0030	0.0163	0.0009	0.0001	0.0013	0.0745	0.0007	0.86	0.6	0.000	0.007	52.9	74.523	0.89
0.20	101.3843	0.0862	1.3033	0.0045	0.0247	0.0009	0.0000	0.0014	0.0535	0.0007	2.88	2.1	0.000	0.002	84.4	76.925	0.37
0.25	149.1962	0.0812	2.0549	0.0064	0.0315	0.0010	0.0000	0.0016	0.0406	0.0007	4.54	3.3	0.000	0.002	92.0	78.198	0.32
0.30	380.6411	0.2001	5.4450	0.0101	0.0760	0.0011	0.0041	0.0016	0.0501	0.0007	12.03	8.8	0.001	0.001	96.1	78.669	0.22
0.35	416.8314	0.1601	6.1361	0.0094	0.0813	0.0012	0.0145	0.0016	0.0206	0.0008	13.55	9.9	0.005	0.001	98.5	78.388	0.20
0.40	389.5881	0.2401	5.7668	0.0090	0.0726	0.0013	0.0000	0.0015	0.0205	0.0010	12.74	9.3	0.000	0.001	98.4	77.891	0.21
0.50	285.9905	0.2001	4.2314	0.0111	0.0546	0.0013	0.0060	0.0015	0.0080	0.0007	9.35	6.9	0.003	0.001	99.2	78.487	0.27
0.60	309.7020	0.2201	4.6144	0.0079	0.0589	0.0013	0.0267	0.0016	0.0094	0.0007	10.19	7.5	0.011	0.001	99.1	77.900	0.22

0.70	366.6239	0.1601	5.4502	0.0082	0.0681	0.0011	0.0067	0.0016	0.0142	0.0008	12.04	8.8	0.002	0.001	98.9	77.879	0.20
0.80	565.3119	0.2401	8.3600	0.0101	0.1096	0.0013	0.0021	0.0015	0.0208	0.0008	18.46	13.5	0.000	0.000	98.9	78.325	0.19
0.90	340.7306	0.2101	5.0602	0.0075	0.0673	0.0012	0.0053	0.0015	0.0075	0.0007	11.18	8.2	0.002	0.001	99.4	78.341	0.21
1.00	230.9470	0.1601	3.4442	0.0063	0.0447	0.0011	0.0018	0.0014	0.0055	0.0007	7.61	5.6	0.001	0.001	99.3	77.980	0.23
1.20	210.1666	0.1501	3.1274	0.0074	0.0397	0.0011	0.0000	0.0014	0.0025	0.0007	6.91	5.1	0.000	0.001	99.7	78.422	0.26
1.50	56.8850	0.0700	0.8476	0.0032	0.0069	0.0006	0.0000	0.0012	0.0011	0.0007	1.87	1.4	0.000	0.003	99.4	78.132	0.45
2.00	181.7443	0.1100	2.6770	0.0068	0.0302	0.0008	0.0000	0.0011	0.0003	0.0008	5.91	4.3	0.000	0.001	100.0	79.441	0.28
4.00	140.5110	0.0990	2.0796	0.0053	0.0244	0.0008	0.0000	0.0012	0.0012	0.0005	4.59	3.4	0.000	0.001	99.7	78.908	0.27
5.00	36.1017	0.0590	0.5262	0.0024	0.0050	0.0007	0.0000	0.0010	0.0008	0.0005	1.16	0.9	0.000	0.004	99.4	79.795	0.52

NOTES:

Samples were irradiated for 3 hours in the central thimble position of the USGS TRIGA reactor. Samples were shielded in cadmium foil. Sanidine from the Fish Canyon Tuff was used as the neutron fluence monitor with a reference age of 28.201 Ma (Kuiper *et al.*, 2008).

Nucleogenic production ratios:

$(^{36}\text{Ar}/^{37}\text{Ar})_{\text{Ca}}$	2.4	$\pm 0.0467 \times 10^{-4}$
$(^{39}\text{Ar}/^{37}\text{Ar})_{\text{Ca}}$	6.587	$\pm 0.103 \times 10^{-4}$
$(^{38}\text{Ar}/^{37}\text{Ar})_{\text{Ca}}$	0.196	$\pm 0.00816$
$(^{40}\text{Ar}/^{39}\text{Ar})_{\text{K}}$	0	$\times 10^{-4}$
$(^{38}\text{Ar}/^{39}\text{Ar})_{\text{K}}$	1.29	$\pm 0.026 \times 10^{-2}$
$(^{36}\text{Ar}/^{38}\text{Ar})_{\text{Cl}}$	3.2	$\times 10^2$
$^{37}\text{Ar}/^{39}\text{Ar}$ to Ca/K	1.96	

Isotopic constants and decay rates:

$\lambda(^{40}\text{K}_{\beta^-})$ /yr	5.81	$\pm 0.17$	$\times 10^{-11}$
$\lambda(^{40}\text{K}_{\beta^-})$ /yr	4.962	$\pm 0.086$	$\times 10^{-10}$
$\lambda(^{37}\text{Ar})$ /d	1.975		$\times 10^{-2}$
$\lambda(^{39}\text{Ar})$ /d	7.068		$\times 10^{-6}$
$\lambda(^{36}\text{Cl})$ /d	6.308		$\times 10^{-9}$
$(^{40}\text{Ar}/^{36}\text{Ar})_{\text{Atm}}$	295.5	$\pm 0.5$	
$(^{40}\text{Ar}/^{38}\text{Ar})_{\text{Atm}}$	1575	$\pm 2$	
$^{40}\text{K}/\text{K}_{\text{Total}}$	0.01167		

#### Appendix 4. K-feldspar $^{40}\text{Ar}/^{39}\text{Ar}$ results

Temp (°C)	$^{40}\text{Ar}/^{39}\text{Ar}$	$^{37}\text{Ar}/^{39}\text{Ar}$	$^{36}\text{Ar}/^{39}\text{Ar}$ ( $\times 10^{-3}$ )	$^{39}\text{Ar}_K$ ( $\times 10^{-15}$ mol)	K/Ca	$^{40}\text{Ar}^*$ (%)	$^{39}\text{Ar}$ (%)	Age (Ma)	$\pm 1\sigma$ (Ma)
11-TR-14, K-spar, 11.53 mg, J=0.0048331 $\pm$ 0.00%									
450	70.50	0.0351	60.718	5.49	14.5	74.6	0.9	408.30	0.93
450	5.932	0.0204	5.263	3.39	25.0	73.8	1.4	37.71	0.30
500	4.013	0.0310	2.326	6.86	16.5	82.9	2.5	28.72	0.17
500	3.296	0.0257	1.689	7.92	19.9	84.9	3.7	24.17	0.13
550	4.003	0.0229	2.042	10.3	22.3	84.9	5.4	29.34	0.12
550	2.801	0.0181	0.913	10.4	28.1	90.4	7.0	21.874	0.099
600	4.464	0.0158	2.466	13.7	32.3	83.7	9.2	32.22	0.11
600	2.851	0.0131	0.651	13.0	39.1	93.3	11.2	22.976	0.076
650	3.617	0.0141	1.423	14.3	36.1	88.4	13.5	27.598	0.090
650	2.766	0.0135	0.399	13.5	37.8	95.8	15.6	22.879	0.075
700	3.323	0.0153	1.057	13.0	33.4	90.6	17.7	25.998	0.085
700	2.995	0.0149	0.444	13.3	34.3	95.7	19.8	24.741	0.072
750	3.574	0.0165	1.133	11.7	31.0	90.6	21.6	27.965	0.097
750	3.419	0.0143	0.601	12.0	35.8	94.8	23.5	27.981	0.085
800	3.973	0.0166	1.386	10.9	30.7	89.7	25.3	30.75	0.11
800	3.903	0.0141	0.953	11.9	36.2	92.8	27.1	31.238	0.096
850	4.391	0.0186	1.828	10.9	27.5	87.7	28.9	33.21	0.11
850	4.299	0.0145	1.411	12.0	35.3	90.3	30.8	33.47	0.10
900	5.018	0.0182	2.577	10.2	28.1	84.8	32.4	36.68	0.13
900	5.008	0.0160	2.477	11.1	31.9	85.4	34.1	36.84	0.13
950	6.048	0.0224	4.182	11.2	22.8	79.6	35.9	41.43	0.15
950	5.716	0.0161	3.153	13.7	31.7	83.7	38.1	41.18	0.13

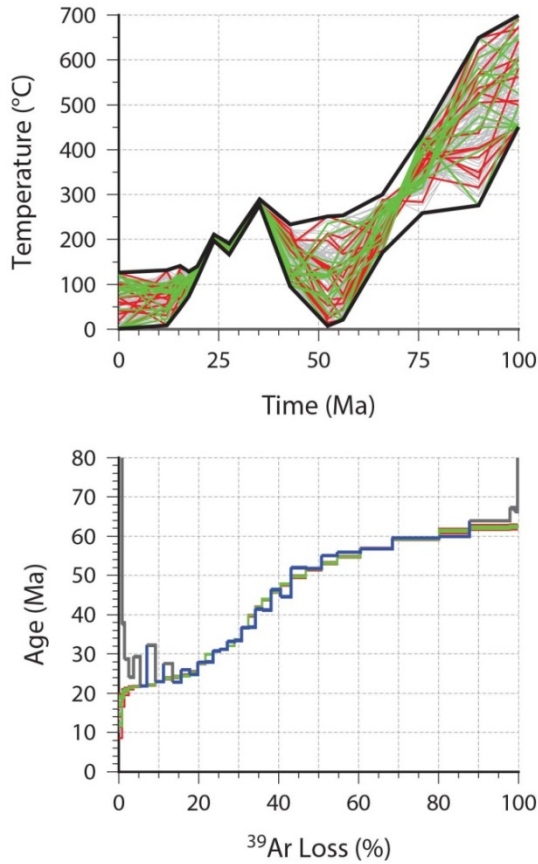
1000	6.379	0.0194	3.306	14.9	26.3	84.7	40.4	46.44	0.12
1000	5.850	0.0175	2.255	17.0	29.2	88.6	43.1	44.59	0.11
1050	6.771	0.0186	2.426	23.2	27.4	89.4	46.8	51.97	0.10
1050	6.665	0.0173	2.131	24.7	29.5	90.6	50.7	51.810	0.091
1100	7.126	0.0212	2.382	24.7	24.1	90.1	54.6	55.09	0.10
1100	7.218	0.0156	2.369	36.7	32.6	90.3	60.4	55.901	0.086
1100	7.260	0.0098	2.158	51.0	51.9	91.2	68.5	56.778	0.076
1100	7.456	0.0064	1.718	73.0	80.3	93.2	80.0	59.520	0.065
1150	7.429	0.0042	1.469	49.3	121.0	94.2	87.8	59.915	0.072
1200	7.839	0.0046	1.258	63.3	110.1	95.3	97.8	63.893	0.071
1250	8.526	0.0093	2.275	8.08	54.6	92.1	99.1	67.15	0.19
1300	8.822	0.0463	3.550	4.16	11.0	88.1	99.8	66.49	0.26
1400	15.54	0.1083	17.834	0.996	4.7	66.1	99.9	87.4	1.1
1650	80.14	0.0473	155.866	0.560	10.8	42.5	100.0	275.1	3.2
<b>Integrated age ± 1σ</b>								50.987	0.049

**11-TR-18, K-spar, 16.22 mg, J=0.0048179 ± 0.00%**

450	22.87	0.0143	15.80	8.11	35.6	79.6	0.6	151.57	0.37
450	3.789	0.0083	1.853	6.47	61.8	85.5	1.0	27.89	0.15
500	6.111	0.0091	4.633	10.3	56.0	77.6	1.7	40.69	0.16
500	2.780	0.0088	0.8352	8.79	58.3	91.1	2.3	21.818	0.099
550	7.165	0.0093	2.416	16.0	55.0	90.0	3.4	55.15	0.13
550	2.534	0.0090	0.4653	12.3	56.7	94.6	4.3	20.650	0.072
600	3.062	0.0100	0.5697	17.0	51.2	94.5	5.4	24.915	0.064
600	2.584	0.0090	0.2702	18.0	56.9	96.9	6.7	21.568	0.046
650	2.889	0.0091	0.2514	22.7	56.0	97.4	8.3	24.238	0.047
650	2.872	0.0081	0.1836	23.1	62.8	98.1	9.9	24.262	0.045
700	3.218	0.0087	0.1923	25.8	58.8	98.3	11.6	27.203	0.050
700	3.320	0.0076	0.1214	28.5	66.9	98.9	13.6	28.256	0.043
750	3.526	0.0079	0.1217	32.1	64.4	99.0	15.8	30.014	0.043

750	3.679	0.0073	0.1238	36.4	70.4	99.0	18.3	31.323	0.043
800	3.974	0.0075	0.1253	37.5	67.7	99.1	20.9	33.830	0.046
800	4.282	0.0065	0.1223	43.6	79.1	99.2	23.9	36.468	0.046
850	4.767	0.0056	0.1233	42.2	91.0	99.2	26.8	40.588	0.050
850	5.260	0.0045	0.1246	51.7	114.2	99.3	30.4	44.773	0.048
900	5.913	0.0037	0.1500	47.5	137.4	99.3	33.7	50.234	0.053
900	6.391	0.0032	0.1627	58.0	159.0	99.3	37.7	54.238	0.049
950	6.964	0.0046	0.2286	49.1	111.3	99.0	41.1	58.903	0.058
950	7.276	0.0051	0.2770	52.2	100.6	98.9	44.7	61.409	0.065
1000	7.860	0.0102	0.4682	37.4	50.3	98.2	47.3	65.835	0.075
1000	8.067	0.0100	0.5476	43.3	51.1	98.0	50.2	67.371	0.073
1050	8.934	0.0159	0.6984	38.2	32.1	97.7	52.9	74.251	0.088
1050	8.908	0.0129	0.6964	47.6	39.5	97.7	56.2	74.038	0.083
1100	9.625	0.0146	0.8286	38.6	35.0	97.5	58.8	79.685	0.094
1100	9.477	0.0092	0.8369	58.2	55.6	97.4	62.9	78.433	0.080
1100	9.417	0.0050	0.8535	81.5	101.7	97.3	68.5	77.887	0.079
1100	9.394	0.0027	0.8675	109.1	186.1	97.3	76.0	77.660	0.069
1150	9.395	0.0019	0.8682	93.3	266.6	97.3	82.5	77.662	0.080
1200	9.164	0.0014	0.7904	211.6	358.7	97.5	97.1	75.935	0.066
1250	9.294	0.0016	0.8315	27.9	325.3	97.4	99.0	76.91	0.11
1300	9.872	0.0033	2.255	4.91	153.2	93.2	99.3	78.23	0.23
1400	10.98	0.0028	3.069	6.02	182.8	91.7	99.7	85.46	0.23
1650	18.90	0.0037	23.38	3.86	138.0	63.4	100.0	101.29	0.55
<b>Integrated age <math>\pm 1\sigma</math></b>								60.966	0.042

**Appendix 5. Representative multi-diffusion domain model results for K-feldspar sample 11-TR-14**



Preferred temperature-time history and modeled vs. measured <sup>40</sup>Ar/<sup>39</sup>Ar spectrum result for sample 11-TR-14. This was selected as the preferred temperature-time history for this sample because it had the best overall fit to the measured age spectrum, did not overconverge, and does not display modeling artifacts encountered in other model runs.

**Input Parameters:**

**CRS Iterations:** 18,000

**Model Duration:** 100 m.y.

**Time Nodes:** 15

**Constraining temp-time brackets:**

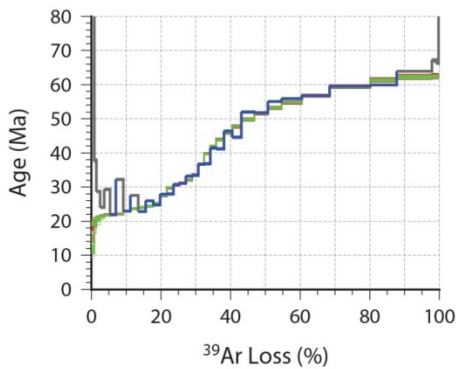
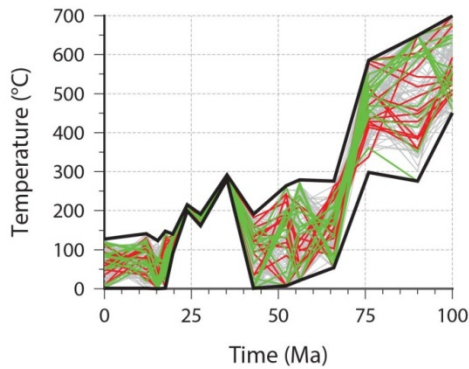
Time	TMin	TMax
100 Ma	450	700
80 Ma	100	600
50 Ma	0	500
25 Ma	0	500
0 Ma	0	250

**Max. Monte Carlo heating/cooling rate:**  
15°C/Ma

**Max CRS heating/cooling rate:** 25°C/Ma

**CRS Amplification factor:** 1.2

**Worst Mean Fit to Age Spectrum:** 2.71%



Temperature-time history and modeled vs. measured  $^{40}\text{Ar}/^{39}\text{Ar}$  spectrum result for sample 11-TR-14 generated by running model stepwise with below input parameters while gradually increasing the allowed Monte Carlo heating and cooling rate (from  $10^\circ\text{C}/\text{Ma}$  to  $60^\circ\text{C}/\text{Ma}$ ). A modeling artifact occurs between 75-100 Ma, where the initial portion of the temperature-time history is poorly-constrained except for a point at  $\sim 70$  Ma.

**Input Parameters:**

**CRS Iterations:** 18,000

**Model Duration:** 100 m.y.

**Time Nodes:** 15

**Constraining temp-time brackets:**

Time	TMin	TMax
100 Ma	450	700
80 Ma	100	600
50 Ma	0	500
25 Ma	0	500
0 Ma	0	250

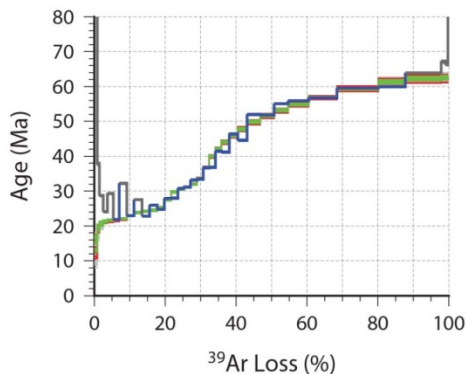
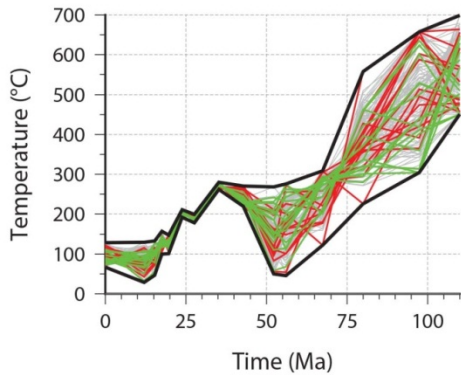
**Max. Monte Carlo heating/cooling rate:**

$60^\circ\text{C}/\text{Ma}$

**Max CRS heating/cooling rate:**  $60^\circ\text{C}/\text{Ma}$

**CRS Amplification factor:** 1.2

**Worst Mean Fit to Age Spectrum:** 2.72%



Temperature-time history and modeled vs. measured  $^{40}\text{Ar}/^{39}\text{Ar}$  spectrum result for sample 11-TR-14 generated by running model stepwise with below input parameters while gradually increasing the allowed Monte Carlo heating and cooling rate (from  $10^\circ\text{C}/\text{Ma}$  to  $45^\circ\text{C}/\text{Ma}$ ) and the CRS heating and cooling rate (from  $15^\circ\text{C}/\text{Ma}$  to  $55^\circ\text{C}/\text{Ma}$ ). Despite the large number of iterations, the histories failed to converge as well as in some other model results.

**Input Parameters:**

**CRS Iterations:** 26,000

**Model Duration:** 110 m.y.

**Time Nodes:** 15

**Constraining temp-time brackets:**

Time	TMin	TMax
110 Ma	450	700
80 Ma	100	600
50 Ma	0	500
25 Ma	0	500
0 Ma	0	250

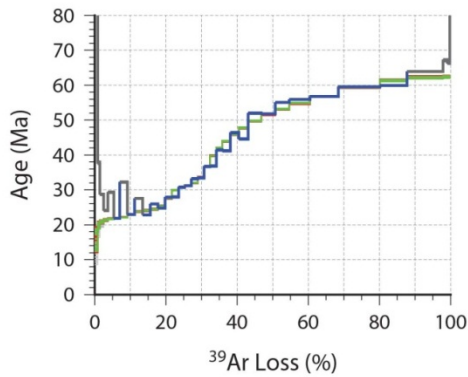
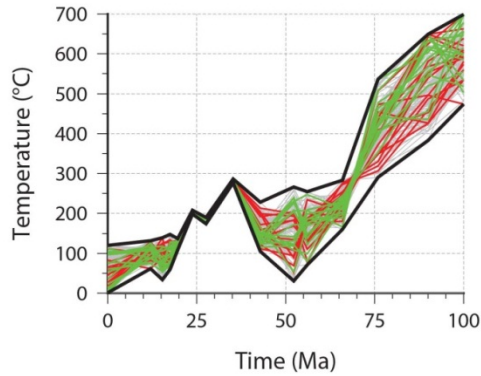
**Max. Monte Carlo heating/cooling rate:**

$45^\circ\text{C}/\text{Ma}$

**Max CRS heating/cooling rate:**  $55^\circ\text{C}/\text{Ma}$

**CRS Amplification factor:** 1.2

**Worst Mean Fit to Age Spectrum:** 2.85%



Temperature-time history and modeled vs. measured  $^{40}\text{Ar}/^{39}\text{Ar}$  spectrum result for sample 11-TR-14.

**Input Parameters:**

**CRS Iterations:** 20,000

**Model Duration:** 100 m.y.

**Time Nodes:** 15

**Constraining temp-time brackets:**

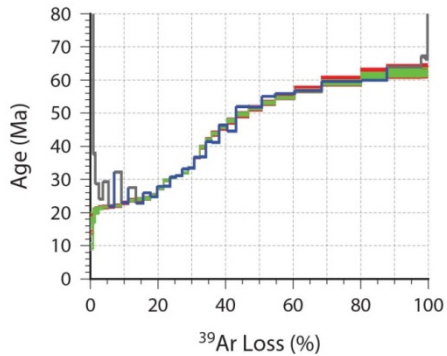
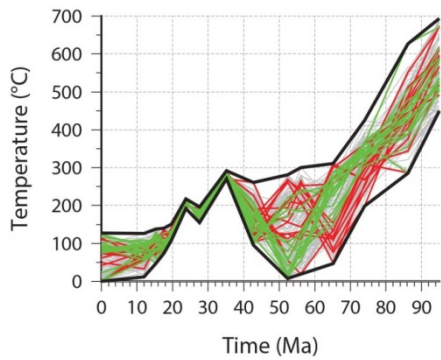
Time	TMin	TMax
100 Ma	450	700
80 Ma	0	600
50 Ma	0	500
25 Ma	0	500
0 Ma	0	250

**Max. Monte Carlo heating/cooling rate:** 5°C/Ma

**Max CRS heating/cooling rate:** 20°C/Ma

**CRS Amplification factor:** 1.2

**Worst Mean Fit to Age Spectrum:** 3.04%



Temperature-time history and modeled vs. measured  $^{40}\text{Ar}/^{39}\text{Ar}$  spectrum result for sample 11-TR-14.

**Input Parameters:**

**CRS Iterations:** 18,000

**Model Duration:** 95 m.y.

**Time Nodes:** 15

**Constraining temp-time brackets:**

Time	TMin	TMax
95 Ma	450	700
75 Ma	75	600
50 Ma	0	500
25 Ma	0	500
0 Ma	0	250

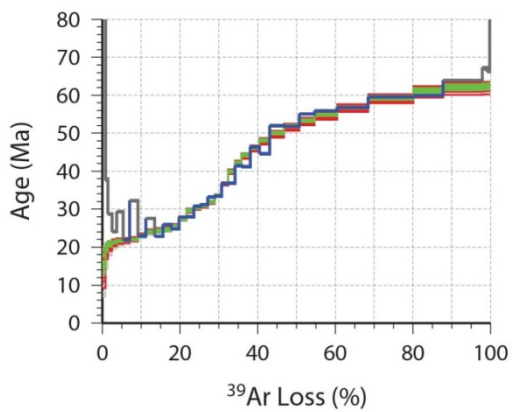
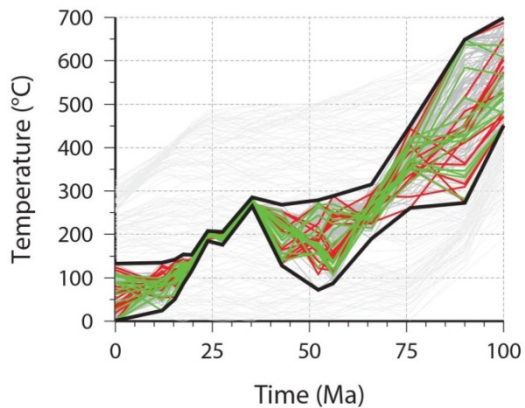
**Max. Monte Carlo heating/cooling rate:** 15°C/Ma

**Max CRS heating/cooling rate:** 25°C/Ma

**CRS Amplification factor:** 1.2

**Worst Mean Fit to Age Spectrum:** 2.89%





Temperature-time history and modeled vs. measured  $^{40}\text{Ar}/^{39}\text{Ar}$  spectrum result for sample 11-TR-14 generated by running model stepwise with below input parameters while gradually increasing the allowed Monte Carlo heating and cooling rate (from  $10^\circ\text{C}/\text{Ma}$  to  $40^\circ\text{C}/\text{Ma}$ ). The thermal histories over-converged between 35-20 Ma, an issue that commonly affected model runs with lower Monte Carlo and CRS maximum heating/cooling rates.

**Input Parameters:**

**CRS Iterations:** 12,000

**Model Duration:** 100 m.y.

**Time Nodes:** 15

**Constraining temp-time brackets:**

Time	TMin	TMax
100 Ma	450	700
80 Ma	100	600
50 Ma	0	500
25 Ma	0	500
0 Ma	0	250

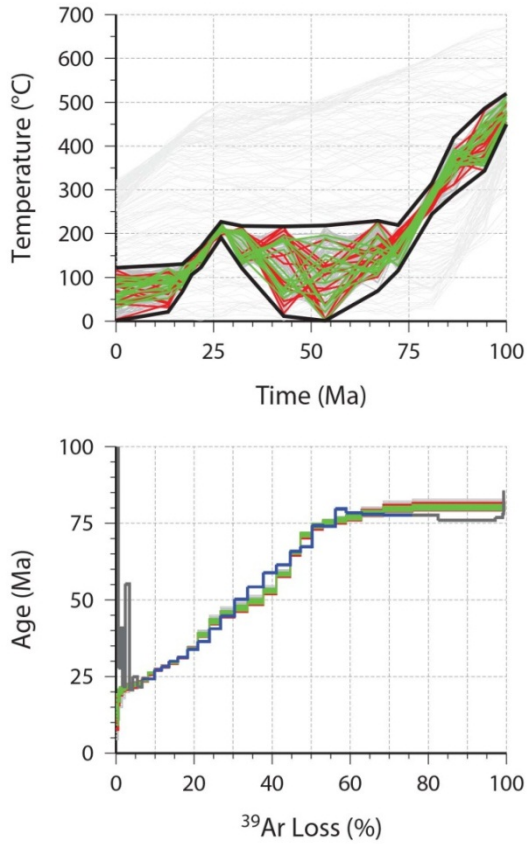
**Max. Monte Carlo heating/cooling rate:**  
 $40^\circ\text{C}/\text{Ma}$

**Max CRS heating/cooling rate:**  $40^\circ\text{C}/\text{Ma}$

**CRS Amplification factor:** 1.2

**Worst Mean Fit to Age Spectrum:** 2.72%

**Appendix 6. Representative multi-diffusion domain model results for K-feldspar sample 11-TR-18**



Preferred temperature-time history and modeled vs. measured <sup>40</sup>Ar/<sup>39</sup>Ar spectrum result for sample 11-TR-18. This sample required more CRS iterations in order to converge properly than sample 11-TR-14. This is the preferred thermal history for this sample because it had a good overall fit to the measured age spectrum, did not overconverge, and does not display modeling artifacts encountered in other model runs.

**Input Parameters:**

**CRS Iterations:** 20,000

**Model Duration:** 100 m.y.

**Time Nodes:** 15

**Constraining temp-time brackets:**

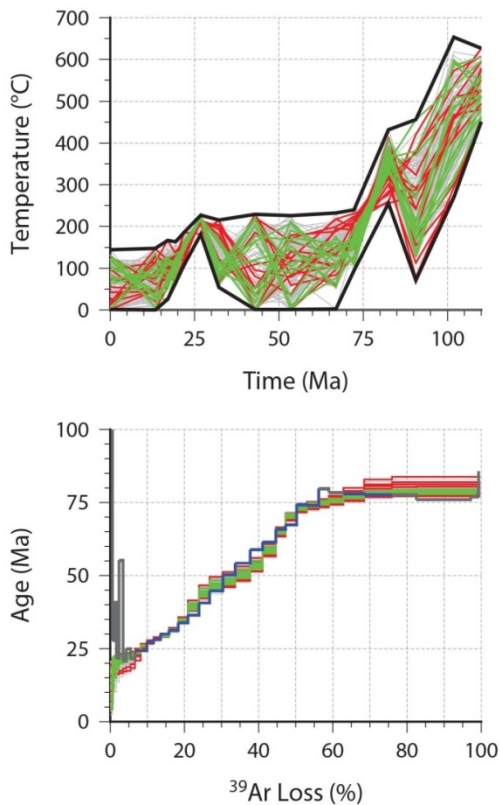
Time	TMin	TMax
100 Ma	450	700
80 Ma	0	600
50 Ma	0	500
25 Ma	0	500
0 Ma	0	250

**Max. Monte Carlo heating/cooling rate:** 5°C/Ma

**Max CRS heating/cooling rate:** 20°C/Ma

**CRS Amplification factor:** 1.2

**Worst Mean Fit to Age Spectrum:** 3.53%



Temperature-time history and modeled vs. measured  $^{40}\text{Ar}/^{39}\text{Ar}$  spectrum result for sample 11-TR-18 generated by running model stepwise with below input parameters while gradually increasing the allowed Monte Carlo heating and cooling rate (from 10°C/Ma to 20°C/Ma) and the CRS heating and cooling rate (from 15°C to 30°C). A modeling artifact occurs between 85-100 Ma, where the initial portion of the temperature-time history is poorly-constrained except for a point at ~85 Ma.

**Input Parameters:**

**CRS Iterations:** 19,000

**Model Duration:** 110 m.y.

**Time Nodes:** 15

**Constraining temp-time brackets:**

Time	TMin	TMax
110 Ma	450	700
90 Ma	0	600
50 Ma	0	500
25 Ma	0	500
0 Ma	0	250

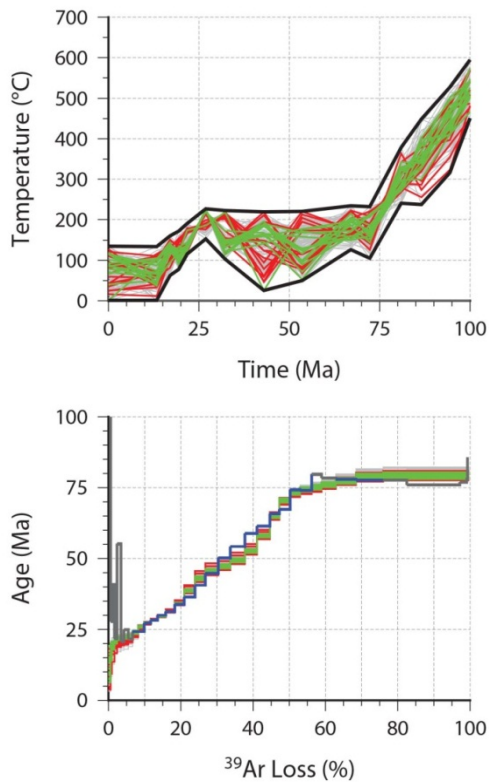
**Max. Monte Carlo heating/cooling rate:**

20°C/Ma

**Max CRS heating/cooling rate:** 30°C/Ma

**CRS Amplification factor:** 1.2

**Worst Mean Fit to Age Spectrum:** 3.91%



Temperature-time history and modeled vs. measured  $^{40}\text{Ar}/^{39}\text{Ar}$  spectrum result for sample 11-TR-18 generated by running model stepwise with below input parameters while gradually increasing the allowed Monte Carlo heating and cooling rate (from 10°C/Ma to 30°C/Ma) and the CRS heating and cooling rate (from 15°C to 35°C).

**Input Parameters:**

**CRS Iterations:** 36,000

**Model Duration:** 100 m.y.

**Time Nodes:** 15

**Constraining temp-time brackets:**

Time	TMin	TMax
100 Ma	450	700
90 Ma	150	600
50 Ma	0	500
25 Ma	0	500
0 Ma	0	250

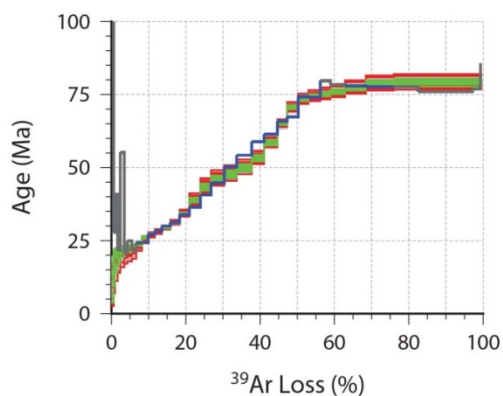
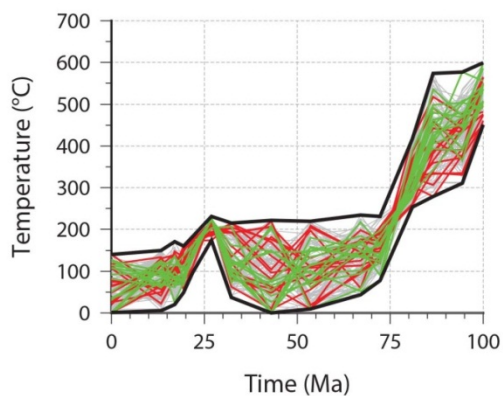
**Max. Monte Carlo heating/cooling rate:**

30°C/Ma

**Max CRS heating/cooling rate:** 30°C/Ma

**CRS Amplification factor:** 1.2

**Worst Mean Fit to Age Spectrum:** 3.72%



Temperature-time history and modeled vs. measured  $^{40}\text{Ar}/^{39}\text{Ar}$  spectrum result for sample 11-TR-18 generated by running model stepwise with below input parameters while gradually increasing the allowed Monte Carlo heating and cooling rate (from 15°C/Ma to 25°C/Ma) and the CRS heating and cooling rate (from 20°C to 35°C).

**Input Parameters:**

**CRS Iterations:** 34,000

**Model Duration:** 100 m.y.

**Time Nodes:** 15

**Constraining temp-time brackets:**

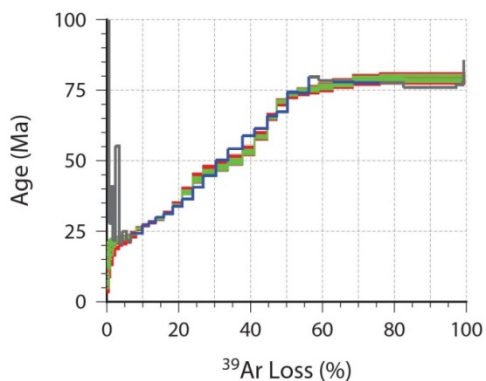
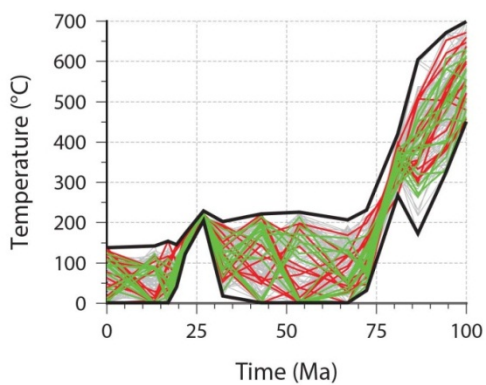
Time	TMin	TMax
100 Ma	450	700
90 Ma	100	600
50 Ma	0	500
25 Ma	0	500
0 Ma	0	250

**Max. Monte Carlo heating/cooling rate:** 25°C/Ma

**Max CRS heating/cooling rate:** 35°C/Ma

**CRS Amplification factor:** 1.2

**Worst Mean Fit to Age Spectrum:** 3.83%



Temperature-time history and modeled vs. measured  $^{40}\text{Ar}/^{39}\text{Ar}$  spectrum result for sample 11-TR-18 generated by running model stepwise with below input parameters while gradually increasing the allowed Monte Carlo heating and cooling rate (from 15°C/Ma to 30°C/Ma) and the CRS heating and cooling rate (from 20°C to 40°C). A modeling artifact occurs between 80-100 Ma, where the initial portion of the temperature-time history is poorly-constrained except for a point at ~80 Ma.

**Input Parameters:**

**CRS Iterations:** 19,000

**Model Duration:** 100 m.y.

**Time Nodes:** 15

**Constraining temp-time brackets:**

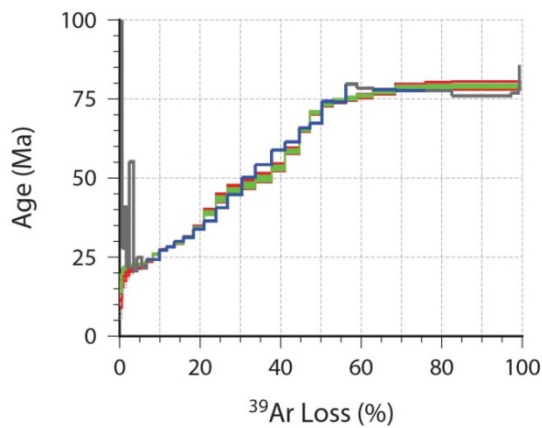
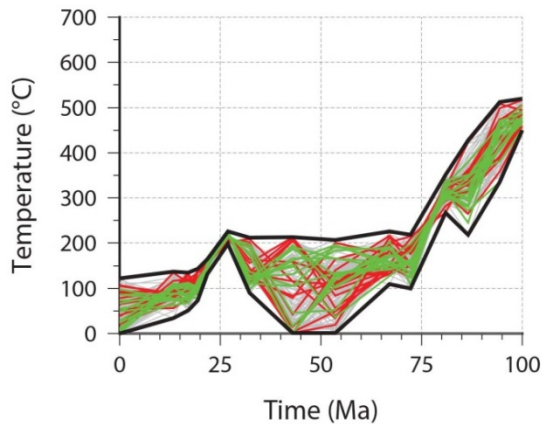
Time	TMin	TMax
100 Ma	450	700
80 Ma	0	600
50 Ma	0	500
25 Ma	0	500
0 Ma	0	250

**Max. Monte Carlo heating/cooling rate:** 30°C/Ma

**Max CRS heating/cooling rate:** 40°C/Ma

**CRS Amplification factor:** 1.2

**Worst Mean Fit to Age Spectrum:** 3.56%



Temperature-time history and modeled vs. measured  $^{40}\text{Ar}/^{39}\text{Ar}$  spectrum result for sample 11-TR-18 generated by running model stepwise with below input parameters while gradually increasing the allowed Monte Carlo heating and cooling rate (from 5°C/Ma to 25°C/Ma) and the CRS heating and cooling rate (from 10°C to 30°C). A modeling artifact occurs between 85-100 Ma, where the initial portion of the temperature-time history is poorly-constrained except for a point at ~85 Ma.

**Input Parameters:**

**CRS Iterations:** 20,000

**Model Duration:** 100 m.y.

**Time Nodes:** 15

**Constraining temp-time brackets:**

Time	TMin	TMax
100 Ma	450	700
80 Ma	0	600
50 Ma	0	500
25 Ma	0	500
0 Ma	0	250

**Max. Monte Carlo heating/cooling rate:** 25°C/Ma

**Max CRS heating/cooling rate:** 30°C/Ma

**CRS Amplification factor:** 1.2

**Worst Mean Fit to Age Spectrum:** 3.41%

## Appendix 7. Apatite (U-Th)/He results

Grain Number	He (pmol)	U (ng)	Th (ng)	Sm (ng)	Th/U (atomic)	raw age (Ma)	$\pm\sigma$ (Ma)	mass ( $\mu\text{g}$ )	mwar ( $\mu\text{m}$ )	U (ppm)	Th (ppm)	Sm (ppm)	eU (ppm)	4He (nmol/g):correction	Ft	Corrected Age (Ma)	$\pm\sigma$ (Ma)	Weighted Mean Age (Ma)
11CAT04_G1	0.00470	0.073	0.005	0.225	0.076	11.75	0.24	1.59	37.00	45.8	3.4	141.5	46.6	2.96	0.674	17.39	0.35	18.40 $\pm$ 0.22
11CAT04_G2	0.00201	0.030	0.017	0.177	0.563	10.78	0.24	1.70	41.75	17.9	9.8	104.5	20.2	1.18	0.683	15.75	0.34	
11CAT04_G3	0.01046	0.121	0.010	0.378	0.084	15.68	0.30	0.86	28.50	140.6	11.5	439.9	143.3	12.16	0.596	26.26	0.51	
11CAT06_G1	0.00259	0.034	0.013	0.176	0.391	12.87	0.31	1.20	32.75	28.5	10.9	147.3	31.0	2.17	0.637	20.15	0.49	20.49 $\pm$ 0.30
11CAT06_G2	0.00137	0.057	0.248	0.074	4.468	2.19	0.05	4.63	57.50	12.3	53.5	15.9	24.8	0.29	0.762	2.87	0.06	
11CAT06_G3	0.00588	0.063	0.029	0.689	0.466	15.43	0.28	3.80	48.25	16.6	7.5	181.5	18.4	1.55	0.743	20.69	0.38	
11CAT07_G1	0.00200	0.009	0.120	0.353	13.235	9.71	0.14	5.59	64.75	1.7	21.5	63.1	6.7	0.36	0.776	12.47	0.18	13.89 $\pm$ 0.13
11CAT07_G2	0.00240	0.027	0.009	0.044	0.355	15.40	0.26	3.38	54.00	7.9	2.7	13.1	8.5	0.71	0.758	20.30	0.34	
11CAT07_G3	0.00195	0.034	0.008	0.306	0.239	9.95	0.17	3.25	50.75	10.5	2.4	94.2	11.1	0.60	0.749	13.25	0.22	
11CAT12_G1	0.00478	0.089	0.014	0.273	0.164	9.61	0.15	1.51	39.50	58.6	9.4	180.0	60.8	3.16	0.685	14.01	0.23	16.37 $\pm$ 0.16
11CAT12_G2	0.00247	0.031	0.026	0.142	0.839	12.15	0.18	0.43	27.75	73.5	60.1	332.4	87.6	5.77	0.553	21.91	0.33	
11CAT12_G3	0.00118	0.026	0.015	0.061	0.586	7.51	0.15	0.33	21.75	77.9	44.5	186.4	88.4	3.59	0.467	16.04	0.32	
11CAT15_G1	0.00213	0.018	0.032	0.044	1.880	15.57	0.24	0.61	27.75	29.1	53.3	71.7	41.6	3.51	0.549	28.30	0.43	25.63 $\pm$ 0.22
11CAT15_G2	0.00776	0.116	0.035	0.072	0.306	11.55	0.21	1.03	34.50	112.8	33.6	69.8	120.7	7.53	0.631	18.30	0.34	
11CAT15_G3	0.00488	0.019	0.116	0.449	6.212	19.23	0.23	0.82	30.50	23.3	140.8	547.5	56.3	5.94	0.571	33.46	0.40	
11CAT16_G1	0.00124	0.004	0.025	0.108	6.639	22.99	0.39	0.76	31.00	5.1	33.0	142.3	12.9	1.63	0.583	39.11	0.67	19.14 $\pm$ 0.18
11CAT16_G2	0.00572	0.064	0.034	0.142	0.549	14.74	0.26	1.04	33.25	61.2	32.7	135.9	68.9	5.49	0.634	23.20	0.41	
11CAT16_G3	0.00266	0.028	0.111	0.442	4.088	8.98	0.12	0.69	27.50	40.4	161.2	639.4	78.3	3.85	0.556	16.07	0.21	
12CAT4D_G1	0.00155	0.025	0.002	0.131	0.062	11.26	0.21	1.54	33.25	16.3	1.0	85.3	16.5	1.01	0.650	17.28	0.32	15.55 $\pm$ 0.16
12CAT4D_G2	0.00198	0.034	0.002	0.155	0.067	10.49	0.19	1.13	30.50	30.3	2.0	137.2	30.7	1.75	0.621	16.85	0.30	
12CAT4D_G3	0.00259	0.044	0.003	0.252	0.075	10.63	0.18	3.58	55.25	12.3	0.9	70.4	12.6	0.72	0.765	13.88	0.23	
12CAT07_G1	0.00230	0.038	0.002	0.218	0.061	10.90	0.19	3.35	53.25	11.5	0.7	65.1	11.6	0.69	0.758	14.35	0.24	15.00 $\pm$ 0.15
12CAT07_G2	0.00249	0.043	0.003	0.221	0.070	10.40	0.18	2.36	48.25	18.4	1.3	93.7	18.7	1.05	0.733	14.16	0.25	

12CAT07_G3	0.00422	0.066	0.010	0.233	0.149	11.43	0.19	1.74	37.75	38.0	5.5	134.1	39.2	2.43	0.671	17.00	0.29	
12CAT8A_G1	0.00401	0.022	0.002	0.193	0.078	33.08	0.55	2.03	44.75	10.7	0.8	95.2	10.9	1.97	0.716	45.99	0.77	
12CAT8A_G2	0	0.001	0.001	0.001	0.660	na	na	0.58	31.50	1.7	1.1	1.3	1.9	na	0.596	na	1.62	37.04 ± 0.47
12CAT8A_G3	0.00152	0.016	0.001	0.073	0.064	16.88	0.32	0.41	25.00	40.0	2.5	177.0	40.6	3.72	0.534	31.45	0.60	
12CAT10A_G1	0.00012	0.004	0.001	0.029	0.246	4.88	0.36	0.52	27.75	8.2	2.0	56.8	8.7	0.23	0.568	8.55	0.64	
12CAT10A_G2	0.00209	0.025	0.003	0.130	0.133	15.28	0.28	1.11	34.50	22.0	2.8	116.5	22.7	1.88	0.648	23.51	0.43	20.26 ± 0.29
12CAT10A_G3	0.00068	0.010	0.001	0.061	0.096	12.59	0.28	0.50	24.75	19.7	1.8	122.4	20.1	1.37	0.539	23.23	0.51	
12CAT11B_G1	0.00522	0.064	0.020	0.243	0.319	14.04	0.23	1.79	35.25	35.7	11.1	135.7	38.3	2.91	0.665	21.07	0.35	
12CAT11B_G2	0.00354	0.046	0.037	0.331	0.823	12.02	0.17	2.33	45.00	19.5	15.7	142.1	23.2	1.52	0.717	16.73	0.24	16.97 ± 0.15
12CAT11B_G3	0.00815	0.106	0.102	0.475	0.993	11.56	0.16	3.00	50.50	35.3	34.2	158.3	43.3	2.72	0.741	15.57	0.22	
ND98_3_G1	0.07098	0.634	0.017	2.923	0.027	20.51	0.30	27.41	88.25	23.1	0.6	106.6	23.3	2.59	0.855	23.87	0.35	
ND98_3_G2	0.00916	0.110	0.003	0.496	0.030	15.32	0.25	5.40	57.75	20.3	0.6	91.8	20.4	1.70	0.774	19.57	0.32	21.31 ± 0.19
ND98_3_G3	0.01106	0.120	0.003	0.498	0.024	16.92	0.26	7.25	67.25	16.5	0.4	68.7	16.6	1.53	0.806	20.93	0.32	
ND01_5_G1	0	0.001	0.001	0.001	1.006	na	na	2.24	35.5	0.6	0.6	0.6	0.8	na	0.674	na	1.24	26.03 ± 0.32
ND01_5_G2	0.00554	0.042	0.062	0.232	1.499	17.88	0.25	0.57	23.75	74.8	109.3	407.7	100.5	9.76	0.533	34.31	0.49	
ND01_5_G3	0.00140	0.022	0.007	0.092	0.317	11.13	0.23	0.42	27.75	50.8	15.7	215.9	54.4	3.28	0.561	19.91	0.42	

## Appendix 8. Plots of AHe age data

